Delft University of Technology

Document Version
Final published version

Citation (APA)
Qin, Z., Soeiro, T. B., Dong, J., Chandra Mouli, G. R., Wang, L., Shi, W., Grazian, F., Yu, Y., & Bauer, P. (2024). Electric vehicle charging technology and its control. In *Control of Power Electronic Converters and Systems: Volume 4* (Vol. 4, pp. 241-307). Elsevier. https://doi.org/10.1016/B978-0-323-85622-5.00014-6

Chapter 9

Electric vehicle charging technology and its control

Zian Qin[1], Thiago Batista Soeiro[2], Jianning Dong[1], Gautham Ram Chandra Mouli[1], Lu Wang[1], Wenli Shi[1], Francesca Grazian[1], Yunhe Yu[1] and Pavol Bauer[1]

[1] *ESE, EEMCS, Delft University of Technology, Delft, the Netherlands;* [2] *PE Group, EEMCS, University of Twente, Enschede, the Netherlands*

9.1 Introduction to electric vehicle charging

The electrification of mobility has an important role in the road map toward a carbon neutral climate by 2050 in Europe and North America, and 2060 in Asia. On the one hand, chargers determine the charging time and thus the user experience. On the other hand, they have a significant impact on the grid [1] and batteries, and thus are an important technology that has received immense attention in both the industry and academia.

According to the power level, electric vehicle (EV) charging is categorized into four modes, standardized in IEC 61851-1 [2], as shown in Table 9.1. As the power level increases, the charging pile configuration changes from single-phase AC to three-phase AC, and eventually DC. This occurs because when implementing charging, a power converter (charger) is needed to convert AC voltage from the grid to the demanded DC voltage of the EV battery. When the power level is low (up to 43.5 kW), the charger is light enough to be installed in the EV (onboard charger), so the charging pile is only a connector, which makes installation easy and inexpensive. In this case, the charging pile outputs AC. However, when the power level is high (above 43.5 kW), the charger is bulky and heavy and is not appropriate for being carried by an EV all of the time. Thus, it is installed in the charging pile (offboard charger). Then, the output of the charging pile is actually the output of the offboard charger, which is DC. An offboard charger is also called a DC charger. A similar definition of charging modes can be found in SAE J1772 (Society of Automotive Engineers) [3], which is the North American standard for EV connectors. The difference is that in SAE J1772, there are only three charging levels, in which levels 1 and 2 are AC onboard chargers and level 3 is the DC offboard charger.

Control of Power Electronic Converters and Systems: Volume 4. https://doi.org/10.1016/B978-0-323-85622-5.00014-6

TABLE 9.1 Charging modes defined in IEC 61851-1 [2].

Charging mode	Configuration	Phase voltage (V)	Max current (A)	Power (kW)
Mode 1	1- phase AC	230	10	2.3
Mode 2	1- or 3- phase AC	230	32	7.4 (1f)/22 (3f)
Mode 3	1- or 3- phase AC	230	63	14.5 (1f)/43.5 (3f)
Mode 4	DC	In development[a]		

[a] *Mode 4 is DC charging. The standards, including ChAdeMO, CCS, GB/T and Tesla supercharger, are developing fast.*

As an interface between the grid infrastructure and the EV battery, the control objective of an EV charger is mainly to achieve high power quality (PQ) (e.g., high power factor and low harmonics) on the grid side and the required charging current (constant current [CC] charging) or charging voltage (constant voltage [CV] charging) on the EV battery side. Therefore, a charger is usually composed of two power stages, a front-end power factor correction (PFC) and a second-stage isolated DC—DC to regulate charging voltage or current and provide galvanic isolation for safety reasons. For onboard chargers, the effort is put into reducing the cost (e.g., bridgeless PFC) [4], and high-power density (e.g., GaN-based charger, a small DC link with active power decoupling) [5—7]. The isolated DC—DC is typically an LLC resonant converter for high efficiency and low electromagnetic interference (EMI). The onboard charger is usually employed in overnight charging (it has a long charging time owing to low charging power). It thus provides a long enough time window to use the EV battery for grid ancillary services, also called vehicle-to-grid (V2G) [8,9]. Table 9.2 lists the charging standards that support the V2X function. V2X is a generic name referring to V2G (grid), vehicle to building (V2B), vehicle to home V2H, and vehicle to load (V2L). V2G is a special case of smart charging, which offers a plethora of opportunities such as the use of EVs to store renewable energy, participate in energy markets, and provide ancillary services. Tesla Model 3 has a bidirectional onboard charger capable of V2G, whereas Nissan has enabled offboard DC chargers for V2G functionality. As a few pioneers have enabled V2G in their chargers, whether onboard or offboard chargers will become the mainstream V2G charger is still the question.

DC chargers have different aims [10]. In DC chargers, isolated DC—DC converters become offboard. Because the charging time is much shorter owing to higher charging power, it will be possible and make sense to share

TABLE 9.2 Various charging standards and their specifications [1].

Standard	CHAdeMO	GB/T	CCS type 1	CCS type 2	Tesla	ChaoJi
Compliant standards	IEEE 2030.1.1 IEC 62916-3	IEC 62916-3	SAE J1772 IEC 62916-3	IEC 62916-3	No related items	CHAdeMO and GB/T (IEC and CCS not yet but ongoing)
Connector inlet						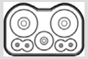
Maximum voltage (V)	1000	750	600	900	410	1500
Maximum current (A)	400	250	400	400	330	600
Maximum power (kW)	400	185	200	350	135	900
Maximum market power (kW)	150	125	150	350	120	N.A.
Communication protocol	CAN		PLC		CAN	CAN
V2X function	Yes	No			Unknown	Yes
Start year	2009	2013	2014	2013	2012	2020

Note: CHAdeMo is developed and more popular in Japan. GB/T is developed and more popular in China. CCS type 1/2 are European standards. Tesla is Tesla's own standard. ChaoJi is the unified standard between China and Japan. *CAN*, controller area network; *PLC*, power-line communication.

the primary side and the transformer of the isolated DC−DC. With the concept of multiplexing, the expense of charging infrastructure is reduced. For DC chargers rated at 200 kW or above, usually a medium voltage transformer is applied to achieve reasonable loss in the grid infrastructure, so the charger is connected to the medium voltage grid via a transformer. To increase the utilization rate of the medium voltage transformer, several DC chargers (e.g., six to ten) are connected to it for sharing. Nonetheless, the transformer has zero or low load over a considerable amount of time per day. To solve this, a battery can be installed in the charging station so that peak charging power will be taken from the battery, whereas the medium voltage transformer as well as the medium voltage grid connection can have a much lower capacity than the total rated power of the chargers. Thus, the expense of charging infrastructure is reduced. A power management control is then needed to coordinate the chargers and battery, ensuring that power taken from the grid is not beyond the capacity of the transformer and the medium voltage cable. In addition, the battery can perform grid support such as voltage control and frequency control, if the DC charger is bidirectional [11].

For charging power at hundreds of kilowatts, the charging gun needs liquid cooling and thus becomes heavy and expensive. Contactless charging is a promising technology for eliminating the charging gun. It also enables charging with the motion of the car [12]. Contactless power transfer includes capacitive and inductive ones, in which the latter is considered to be more promising for contactless EV charging. An inductive contactless charger has a power conversion structure similar to the onboard/offboard charger, but the charger is split into two parts from the isolated transformer, and the transformer is replaced with two charging panels with a coil and magnetic core. One charging panel is onboard whereas the other is offboard. Because the primary and secondary sides are contactless, feedback of signals from the secondary side to the primary side relies on wireless communication. Accordingly, control of contactless chargers is categorized into three groups: primary side, secondary side, and dual side. In primary side control, only the primary side converter is controlled. Still, the required current or voltage of the load measured on the secondary side will be sent to the primary side controller via wireless communication. In secondary side control, the primary side converter operates in an open loop and only the secondary side converter is controlled to fulfill the load requirement. No wireless communication is needed in this scenario. In dual-side control, both sides are controlled and wireless communication is used for feedback or feedforward signals, in which the load is properly powered and the primary side is well-controlled to match the load, thus minimizing the loss of the whole power conversion [13−15].

The installation of chargers (both low and high power) is increasing dramatically with huge market demand. Whether the operation of the grid infrastructure is robust enough to handle this large amount of integration is still questionable. In fact, a few PQ issues in terms of voltage imbalance, flicker, harmonics, and supraharmonics have been reported, which are associated with high-power EV chargers nearby [16—18]. However, PQ standards dedicated to EV charging do not yet exist. The current practice is to refer to the IEEE PQ standards [19—22] and IEC 61000 series [23—31], which are widely used in PQ evaluation. PQ issues can generally be categorized into problems with the voltage level, voltage fluctuation, voltage unbalance, harmonic current distortion, harmonic voltage distortion, and so on. A few mitigation measures can be found in the literature or have been applied in practice to perform PQ in compliance with these standards, such as real-time charging navigation frameworks to overcome the impact of fast charging on voltage stability [32] and fast charging station management to regulate charging power according to grid conditions [33]. Impedance-based approaches have become the norm in the harmonic evaluation of grid-tied power electronics [34—36], including EV chargers. Input impedance modeling of EV chargers has been carried out in the literature [37,38]. Because the input impedance of EV chargers is significantly affected by control parameters, it can be properly shaped to mitigate harmonics as well as to enhance stability [39,40].

With the argument that the EV is green only if the electricity used for charging is from renewables, the integration of PV systems into EV charging stations is drawing increasing attention. Because photovoltaic (PV) power generation does not naturally match EV charging power, it is preferable for battery energy storage to be installed in the charging station as a buffer to smoothen power drawn from the grid. In this scenario, a power management strategy is needed for the battery. Moreover, considering the PV, EV, and battery as a whole system, the power conversion stage can be simplified and made more compact and efficient. A multi-active bridge converter with inherently decoupled power flows is a promising converter design for this application [41], because power transmission between the slack bus (a battery or grid) and any port would not affect power delivery in another port. This can be implemented with simple phase shift control [41,42].

The primary layer control of the EV charging is the charging current/voltage control. Moreover, the whole charging process can be controlled (not yet implemented in most chargers, but the current charging infrastructure is capable of doing it) in terms of ramping up or down time, charging power, charging time window, and so forth. A series of intelligent controls for this objective is smart charging, which has the potential to increase the utilization rate of the grid infrastructure, reduce the charging cost with the flexible price of electricity, increase efficiency in power transfer, reduce the impact on the grid, and increase system autonomy, especially when renewables are integrated into the charging station.

In the next part of this chapter, more details are given in terms of power converter topologies and control of onboard and offboard chargers, contactless charging, PQ of EV charging, integrating renewables in charging stations, and smart charging algorithms and protocols.

9.2 Onboard charger

Onboard chargers are widely used because the charger exists in the EV and only a grid connection is needed. In this section, onboard charger technologies will be reviewed in terms of the converter topology and control. Because the onboard charger is usually composed of a single-phase AC−DC converter, instant power imbalance between the AC and DC sides has to be well taken care of. Therefore, the advanced approach of active power decoupling is also reviewed.

9.2.1 Conventional power electronics and feedback control strategy

The main power electronic circuit of an onboard charger is typically a single-phase connection in which a two-conversion stage system is employed. An exemplary circuit is shown in Fig. 9.1, in which the front-end (or grid-

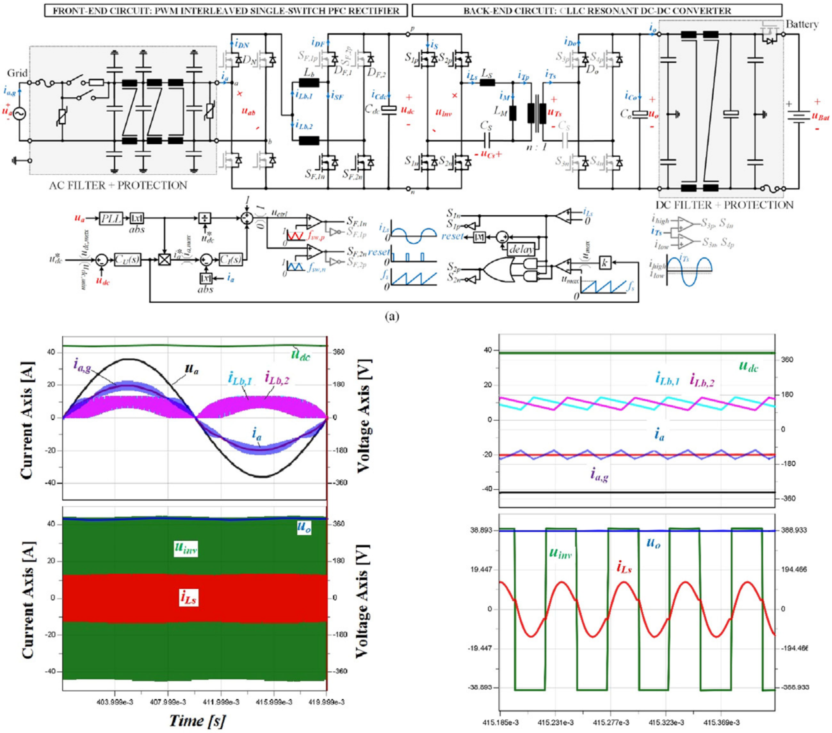

(a)

(b)

(c)

FIGURE 9.1 Conventional two-stage onboard electrical vehicle charger based on single-phase three-level bridgeless rectifier and LLC (or CLLC) resonant DC−DC converter: (A) main schematic and feedback control strategy; (B) Main simulation results within a grid period; (C) Waveform zoom. *PFC*, power factor correction.

connected) circuit provides PFC operation to fulfill grid harmonic standards, whereas the required battery galvanic isolation from the grid is enabled at all times by the back-end converter. The PFC circuit is conventionally designed and controlled to supply to the back-end circuit a relatively stable and nearly constant DC-link voltage (u_{dc}) by absorbing power fluctuations resulting from the single-phase AC−DC conversion. Therefore, this circuit may adopt a large (electrolytic-based) DC-link capacitor (C_{dc}), which can (advantageously) decouple the control loop dynamics of the front- and back-end circuits. The back-end circuit may provide the charging profile requested by the EV battery stack with a suitable current control, for which a low current ripple is necessary.

In the example of Fig. 9.1, the onboard charger is composed of a single-phase two-channel pulse width modulation (PWM) interleaved single-switch PFC rectifier cascaded with an LLC (or CLLC) resonant DC−DC converter. Both power electronics circuits are known for their simplicity, low cost, and relatively high power efficiency. In parallel with all diodes of unidirectional grid-to-battery power conversion, a MOSFET (in gray) can be added to improve conduction losses of the circuit and/or to allow power transfer from the EV battery to the grid (or V2G). For V2G operation, the addition of a series AC capacitance to the secondary side of the high-frequency transformer in the back-end converter could be advantageous to avoid saturation of the transformer (i.e., one would change the LLC into a CLLC resonant converter). The feedback control loop shown in Fig. 9.1 implements a basic PFC feedback control scheme with a cascaded outer voltage loop (slow) and inner AC loop (fast). The back-end circuit implements the dual control [43], in which the operating switching frequency is automatically adjusted to ensure that the operation of one bridge leg takes place close to the zero current crossing of i_{Ls} at full duty cycle d, whereas the other bridge is controlled at the same frequency but with duty cycle management to control the battery current or voltage.

The LLC resonant converter control can be tuned to operate the H-bridge inverter mostly at maximum duty cycle ($d \sim 0.5$ or bipolar modulation) with a switching frequency close to the equivalent series resonant frequency of L_S and C_S. Thus, the equivalent system voltage gain is decoupled from the converter power loading and is mainly defined by the transformer turns ratio n [44]. This operating principle is interesting because it makes the isolated DC−DC converter behave as an electronic DC transformer, in which the high-frequency inverter works at a high power factor (i.e., low reactive power circulation), which will lead to low conduction and switching losses in the circuit. This is also known as an optimum load operation. For the LLC resonant converter, the advantageous zero voltage switching (ZVS) turn-on for the H-bridge semiconductors is safeguarded by the design of the parallel inductance L_M. This provides the means to make the circuit operate in the equivalent inductive region of the resonant tank so that the MOSFETs' parasitic drain-to-source capacitances within a half-bridge can be fully charged and discharged before each device is turned on.

For the battery charger to function effectively while the LLC converter operates under optimum load conditions at a wide range, the PFC circuit must take control of the system providing the necessary battery charging profile (e.g., CC and CV) [45]. Hence, DC-link voltage u_{dc} must be designed to withstand a voltage range between a minimum ($u_{dc,min}$) and maximum value ($u_{dc,max}$), which covers the whole battery voltage range. This can work because u_{dc} is closely related to battery voltage u_{Bat} because in the optimum load operation the resonant converter voltage gain is nearly constant and independent of the power loading of the system. This also suggests that AC side current i_a has an intrinsic relationship to battery current i_o ($P_{in} \sim P_{BOI}$). Thus, limiting i_a to a maximum value $i_{a,max}$ within the feedback control loop can guide the charging profile to a CC operation. The CV operation is controlled by setting up an appropriate voltage loop reference, u_{dc}*, or limiting value $u_{dc,max}$ slightly higher than the battery fully charged voltage.

Fig. 9.1B presents the simulation results of the conventional EV charger, in which power is delivered from a single-phase 230 V RMS (root mean square) (phase-to-neutral)/50 Hz grid to a 400-V battery class. Both the front- and back-end circuits are able to operate according to their intended principles (i.e., high power factor and symmetric PWM interleaved operation for the front-end circuit, and ZVS turn-on for the MOSFETs and high-frequency H-bridge inverter operating close to the series resonance with a maximum duty cycle). Fig. 9.2 shows an 11-kW LLC resonant converter designed as a power electronics building block (PEBB) of an EV charger by TU Delft. Although the circuit uses silicon (Si) IGBTs and diodes, the peak efficiency is relatively high and close to 98.3% at 6.5 kW operation. The experimental waveforms at the point of maximum efficiency are shown in Fig. 9.2B.

9.2.2 High-performance power electronics circuits for onboard chargers

To reduce conduction losses across semiconductors of the PFC rectifier stage, bridgeless circuit technology can be used. Fig. 9.3A and B show two conventional bridgeless PFC circuits; other topologies can be found in Lange et al. [4]. In the bridgeless circuits in the illustrations, only two semiconductors at each time will conduct the inductor L_b impressed current. The basic cell of the single-switch PFC circuit shown in Fig. 9.1 always has three semiconductor devices conducting current in every operation stage. The main drawback to the bridgeless circuits depicted in Fig. 9.3A and B is the common-mode floating of the DC-link bus in relation to the grid neutral point, which demands more complex EMI filtering for grid compliance. The full-bridge rectifier employing unipolar switches depicted in Fig. 9.3C could further reduce semiconductor conduction losses because of the equivalent resistive loss behavior of the

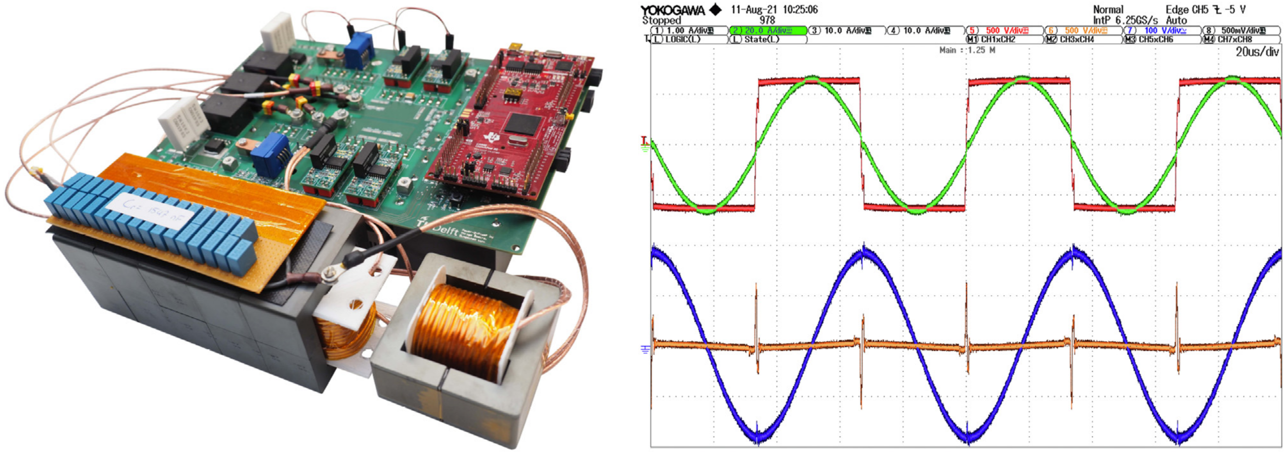

(a) (b)

FIGURE 9.2 (A) Hardware setup of 11-kW LLC resonant DC−DC converter; (B) Main experimental results at point of highest efficiency. The power processed is 6.5 kW, whereas the input and output voltages are 640 and 400 V, respectively. The switching frequency is set to 16 kHz, which is close to the resonant frequency. For the experimental waveform, resonant current i_{Ls} is the sinusoidal *green* curve at the top at 10 A/div; the voltage across the series capacitor u_{Cs} is the sinusoidal waveform in *blue* at the bottom at 100 V/div; the inverter output voltage u_{inv} is the square *red* wave at the top at 500 V/div; and the voltage across L_S and C_S is the bottom *orange* curve at 500 V/div. For interpretation of the references to color in this figure legend, please refer online version of this title.

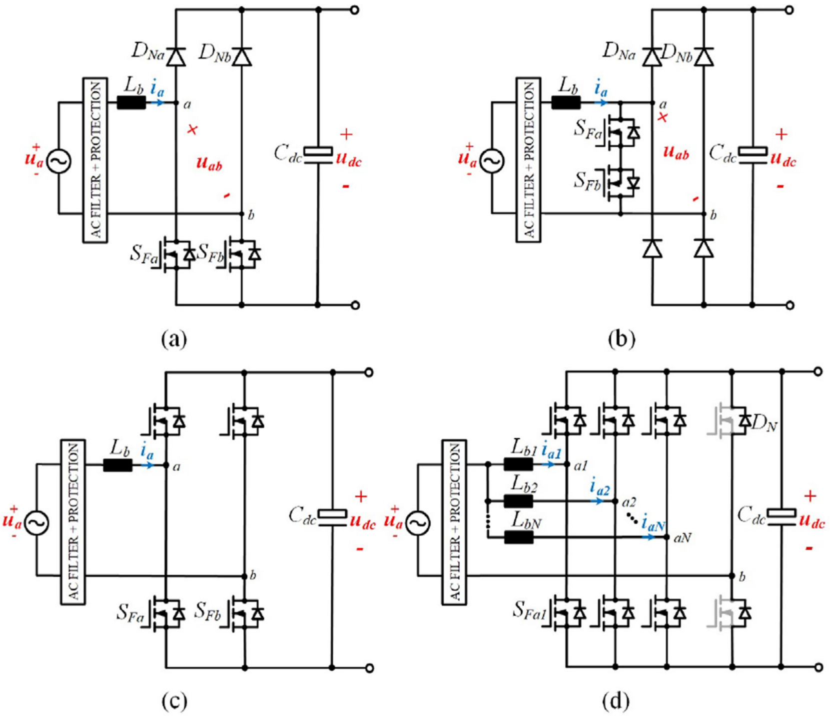

FIGURE 9.3 Single-phase power factor correction rectifiers: (A, B) Conventional bridgeless technology; (C) Full-bridge rectifier; (D) PWM interleaved totem pole rectifier.

unipolar devices. The antiparallel bipolar device (the body diode of the MOSFET) will conduct only during the required dead time (i.e., for approximately 200 ns). Thus, dead time is necessary to avoid the destructive short-circuit of the DC-link. In bridgeless circuits, the diodes protect the circuit from this fault condition.

The full-bridge converter depicted in Fig. 9.3C also constitutes a good solution for a V2G application, but operation of the circuit with unipolar modulation (or a three-level voltage source operation), which is advantageous for minimizing differential noise generation, will also have the problem of a floating DC-link in relation to the grid worsening the common-mode noise injection. Bipolar modulation (or a two-level voltage source operation) will have superior common-mode noise generation but worse differential mode noise generation.

The totem-pole PFC rectifier depicted in Fig. 9.3D features the advantage of the bridgeless circuit in terms of minimized semiconductor conduction losses. While operating at a high power factor, it also requires smaller common-mode EMI filtering because diode bridge D_N will connect the

DC-bus to the AC terminal according to the polarity of the grid voltage (low-frequency operation). In the circuit shown in Fig. 9.3D, the high-frequency switching half-bridges are split into several PWM interleaved circuits that can be advantageously operated in a triangular current mode (TCM) [46] to guarantee ZVS turn-on of the semiconductors.

9.2.2.1 Universal single- and three-phase power factor correction front-end circuit

The market for EV charging is global. Hence, developing a single hardware solution that satisfies a plurality of markets without the need to overdimension circuit components gives a competitive advantage to the manufacturer. However, this is challenging because the power electronics would need to cope with different electricity grids and their standards. For example, a high-power onboard charger aiming at 19.2–22 kW power capability would need to be operated in a single-phase 240 V/80 A grid in the United States or Japan, or a three-phase 400 V/32 A grid in Europe. In Papamanolis et al. [47] a universal front-end PFC rectifier was proposed that enables a high charging power at a level rated for both the US single-phase and European three-phase grid supply without overdimensioning the active semiconductor, which accounts for most of the cost of the converter. The main idea is to add a high-current diode bridge to the conventional three-wire, two-level voltage source rectifier (2L-VSR) that would be mainly designed for the European market. The current rating of the line frequency diode would be rated to three times that from active semiconductors, but this has a much lower cost figure. In addition, a modification on the typical common-mode stage filter designed for the three-phase, three-wire power delivery would be necessary to avoid saturating the common-mode inductor in the single-phase operation. A similar circuit is shown in Fig. 9.4, in which the necessary change for operating in the single-phase market is highlighted in red. The single-phase configuration matches the totem pole rectifier technology depicted in Fig. 9.3D. Moreover, without the addition of the diodes, the single-phase operation could be implemented using two active bridges, but this would limit the circuit power rating to one-third the rated power of the three-phase circuit.

In Fig. 9.4, the feedback control loop shown is suitable for the TCM operation of the PWM interleaved totem pole rectifier. The phase locked loop (PLL) is used to obtain the fundamental 50- or 60-Hz component of the grid voltage, which is later used to derive the AC current reference and the variable switching frequency $f_{sw,x}$, which is necessary for the TCM operation. The latter is calculated based on the required turn-on and -off times of the half-bridge switches, which will depend on the rectifier's AC input and DC output voltages, the generated AC current reference i_a*, and the reverse current I_R* required to achieve the ZVS turn-on of the MOSFETs. The back-end converter constitutes a phase-shift forward-based converter that will be responsible for

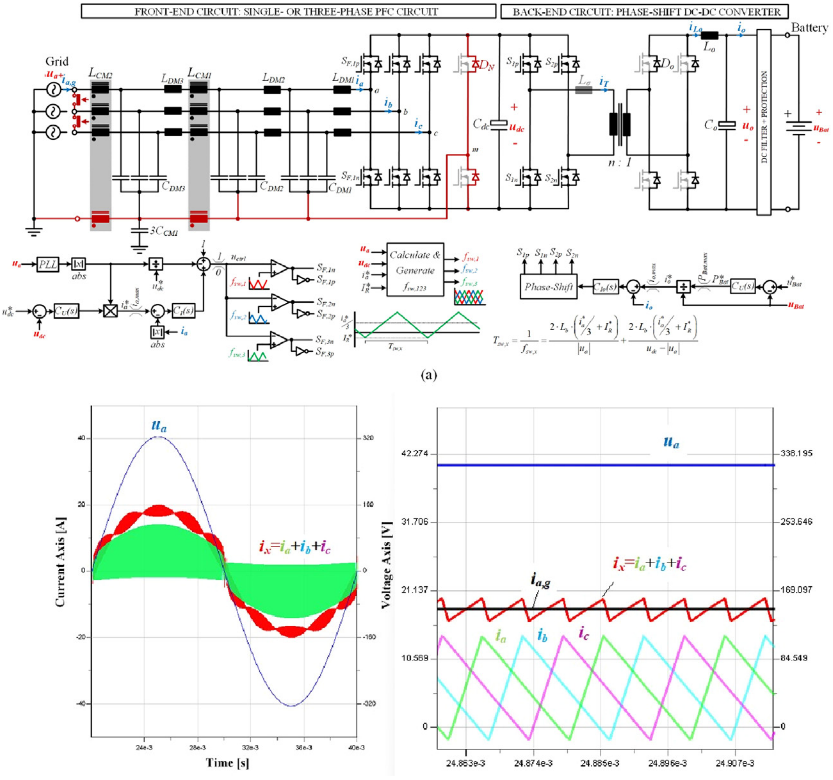

(a)

(b)

(c)

FIGURE 9.4 (A) Universal single- or three-phase front-end power factor correction (PFC) rectifier and suitable electromagnetic compatibility filter for onboard electric vehicle charger for US and European markets. Compared with a conventional three-phase, three-wire, two-level voltage source rectifier, the added components (in *red* (gray in print)) allow full power delivery for both single- and three-phase operations (i.e., in US and European markets); (B) Main simulation result for single-phase PFC operation and PWM interleaved triangular current mode within a grid period; (C) Waveform zoom. *PLL*, phase locked loop.

controlling the battery charging profile. Implementation of the phase-shift modulation is discussed in Lyu et al. [45]. It is used to adjust the equivalent duty cycle of the isolated converter. Fig. 9.4B shows the simulation results for the TCM operation of the active front-end circuit. The circuit draws a high–power factor operation. Fig. 9.5 shows an 11-kW phase-shift forward converter in a current doubler configuration designed as a PEBB of an EV charger by TU Delft. Although the circuit implements Si IGBTs and diodes, the peak efficiency is relatively high and close to 97.6% at 11 kW operation. Experimental waveforms at the point of maximum efficiency are shown in Fig. 9.5.

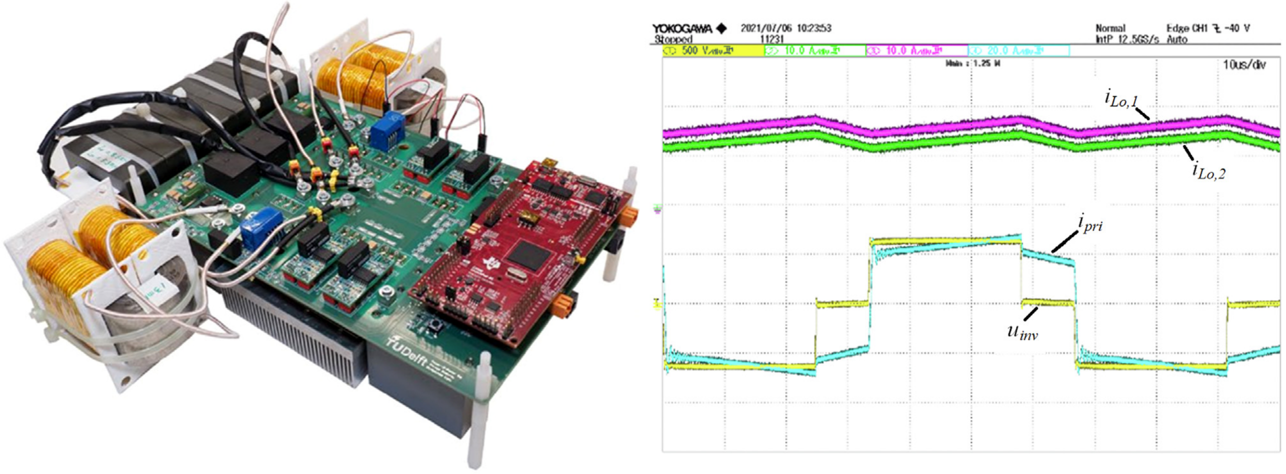

(a) (b)

FIGURE 9.5 Hardware setup of phase-shift forward-based current doubler DC–DC converter, and main experimental results at the point of highest efficiency. The power processed is 11 kW, whereas input and output voltages are 640 and 400 V, respectively. The switching frequency is set to 16 kHz. In the experimental waveform, the two output inductor currents are summed in the current doubler operation as i_{Lo} (pink and green curves that are the two top curves at 10 A/div), the primary side transformer current (*blue* at 20 A/div), and inverter output voltage u_{inv} (*yellow* at 500 V/div). For interpretation of the references to color in this figure legend, please refer online version of this title.

9.2.2.2 Bidirectional single-phase power factor correction rectifier and active power decoupling circuit

The inherent ripple power in the single-phase converter results in an undesirable low frequency ripple on the DC-link, which can reduce both the PQ at the AC grid and system reliability [48]. In conventional PFC systems described in the previous section to address this issue, a large energy storage device is used, such as a bulky electrolytic capacitor to passively smoothen the power oscillation. This will result in a bulky converter and the potentially reduced lifetime of the system.

To reduce the requirements of the DC capacitor bank, active power decoupling techniques can be used. This offers an alternative path for the ripple power to flow through by using extra energy storage components such as capacitors or inductors and auxiliary power switches, enabling a considerable reduction in the requirement of smoothing capacitors on the DC-link. An example of an AC-type decoupling method is shown in Fig. 9.6. This AC-type half bridge—based active power decoupling method with an auxiliary storage capacitor connected between the extra half-bridge and another of the single-phase full-bridge converter is a popular choice owing to the reduced components and less current and voltage stress on the additional circuit components [48].

The auxiliary power decoupling circuit adds extra power losses to those caused by the operation of the conventional full-bridge converter, which will inevitably reduce the system power conversion efficiency. To relieve this shortcoming, Xu et al. [7,48] proposed a discontinuous PWM (DPWM) strategy with minimum switching losses, which is particularly interesting for bidirectional full-power factor (V2G operation) single-phase PFC converters associated with the AC-type half-bridge active power decoupling circuit. The control and circuit topology are shown in Fig. 9.6A and B, respectively. The control algorithm emulates the operation of a three-phase voltage source converter operating with unbalanced AC voltages. This is able to detect the current measurements and the converter voltage references, and it instantaneously determines the optimal clamping duration in each phase. With such a characteristic, the control strategy can realize minimal switching losses at any instant, improving power efficiency, which will be superior to traditional SVPWM (Space Vector PWM) or DPWM methods available in the literature (e.g., those used in symmetric three-phase, three-wire applications) [49].

Fig. 9.6C and D present a 2-kVA hardware demonstrator of the power electronics depicted in Fig. 9.6A and the experimental results obtained for a rectifier operation while implementing the control algorithm illustrated in Fig. 9.6B. In this case, the DC-link is controlled to be at 400 V, whereas the circuit is fed by a 220-V RMS (phase-to-neutral)/50 Hz grid. A relatively low DC capacitance is used in the circuit (i.e., $C_{dc} = 135$ pF). Thus, a large DC voltage ripple will be found without the operation of the active power

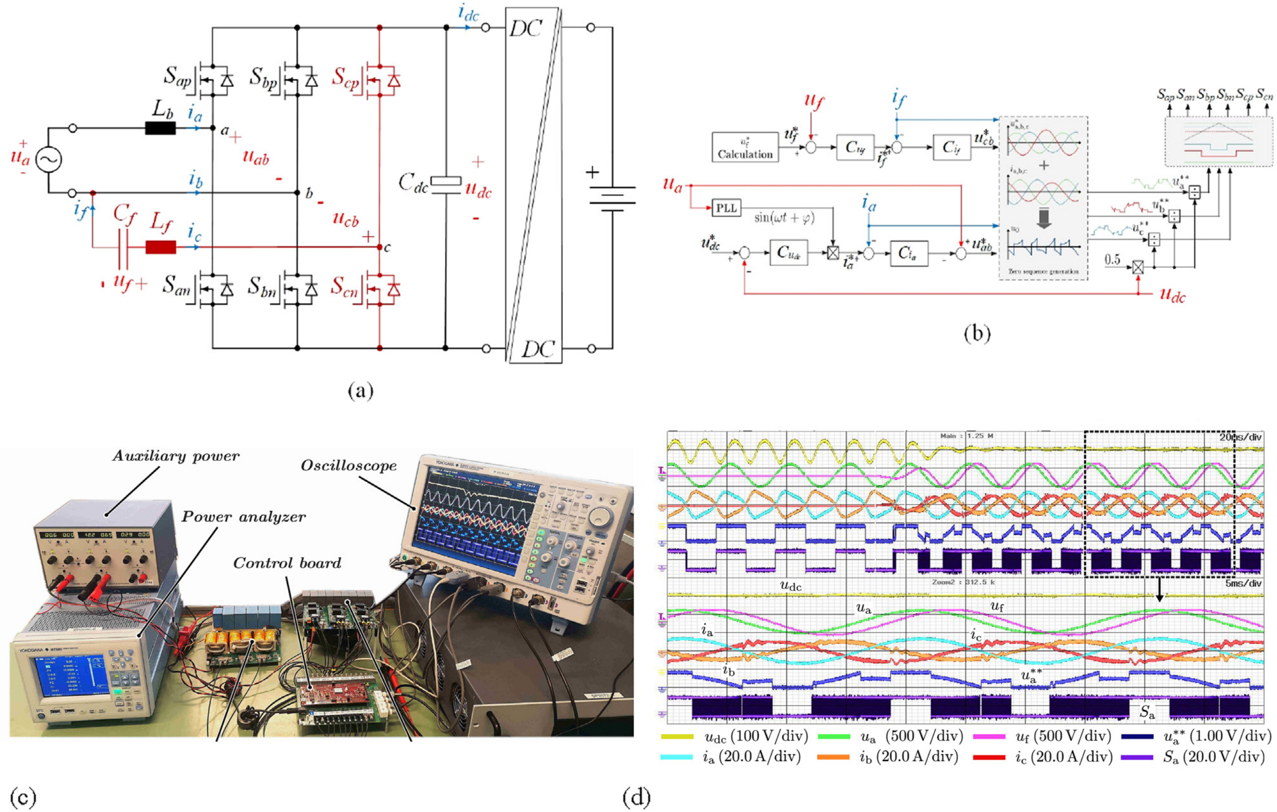

FIGURE 9.6 Active power decoupling circuit: (A) Circuit schematic; (B) Control block diagram of bidirectional single-phase power factor correction rectifier plus AC-type active power decoupling circuit featuring minimal switching loss discontinuous PWM modulation. (C) Experimental setup; (D) Results for rectifier operation, in which the transient shows enabling of an active power decoupling circuit. (D) Zoom function of the oscilloscope is used to show details of the highlighted section of experimental waveforms. *PLL*, phase locked loop.

decoupling circuit. To verify the advantage of the circuit concept in Fig. 9.6D, the experimental waveforms present results before and after the active power decoupling circuit is enabled. With the insertion of the active power decoupling circuit and the incorporated AC power compensation components, the ripple in the DC voltage is remarkably reduced and the AC current waveform shape is improved. More details about this circuit concept can be found in Xu et al. [7,48].

9.3 Offboard charger

For AC-type EV chargers, DC-types, which are placed offboard the vehicle, are typically implemented as a two-stage system composed of a PFC rectifier as the front-end converter followed by a DC−DC converter. In Europe, for currently available public high-power charging infrastructures (e.g., $P_o > 50$ kW), DC-type chargers, also called fast, semifast, or ultrafast chargers, are dominant. Fig. 9.7 shows a typical high-power EV charging station.

Galvanic isolation of the car battery to the AC grid or between different vehicles is needed for safety reasons. This can be provided by an isolated DC−DC converter and/or a line frequency 50/60-Hz transformer at the grid side [10]. In high-power charging stations (e.g., $P_o > 100$ kW), multiple EVs can be recharged by the same power electronics (i.e., by different isolated DC−DC converters fed by the same DC-link bus), and thus both galvanic isolation options may be employed. This is because for higher power infrastructures, a connection to the medium-voltage (MV) AC grid may be

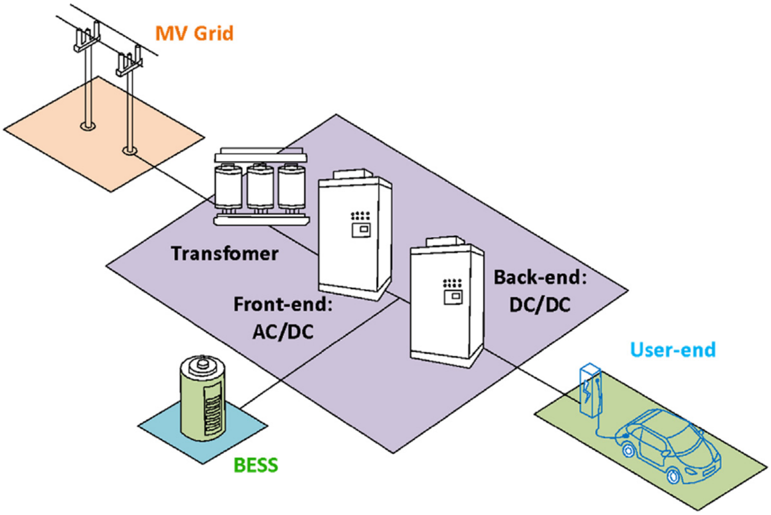

FIGURE 9.7 Typical high-power electric vehicle charging station with integrated battery energy storage system (BESS). *MV*, medium-voltage.

necessary through a line frequency transformer or solid-state transformer (SST) [117] because of the power limitation on the low-voltage public distribution grid.

From the charging infrastructure owner's perspective, to counteract the expected reduction in governmental subsidies and consequent increase in charging costs, the system could incorporate battery energy storage systems (BESS) into the charger's inner DC-grid and/or renewable energy generation, such as photovoltaic strings installed on the rooftop of charging stations. This is advantageous for buffering the power demand from the AC grid and reducing energy consumption costs. This also allows for participation in the network ancillary service market, generating extra profits for stakeholders [11]. From the power electronics manufacturer's perspective, the system conceptualization using PEBB is advantageous. Output power and voltage scalability are vital features for dynamic power electronics markets. This leads to manufacturing cost advantages (or the low investment of pounds per kilowatt, because a single circuit building block design (e.g., $P_o = 11-25$ kW) can satisfy a plurality of business applications from several kilowatts up to megawatt solutions.

From the perspective of user convenience, the EV battery should be recharged in the shortest time possible. Therefore, fast DC-type EV chargers are mainly designed for unidirectional power flow (i.e., grid-to-vehicle) and may process only limited reactive power for grid support, i.e., power factor $> \pm 0.87$. In this case, when a BESS is not necessary, the system can take advantage of the typical lower circuitry complexity and higher reliability found in unidirectional power electronics. For example, the PFC rectifier stage can be based on the unidirectional two-level delta-switch voltage source rectifier (DS-VSR) proposed in Kolar et al. [50], cascaded with a buck-type DC–DC converter, as depicted in Fig. 9.8A. The simple buck-type converter can be used as the back-end converter only if the infrastructure charges only one vehicle at a time. For multiple vehicle charging, isolated DC–DC converters are necessary owing to galvanic isolation requirements. Nevertheless, the performance of the DS-VSR circuit can be comparable to the conventional bidirectional 2L-VSR depicted in Fig. 9.3. DPWM modulation with 120 degrees clamping interval per phase leg often used in the three-wire 2L-VSR [49] can also be adapted to the DS-VSR as presented in Hartmann et al. [51] and Soeiro et al. [52]. This enables the front-end system to show reasonable power efficiencies, which may be comparable to the three-level unidirectional VIENNA-type rectifiers proposed in Kolar and Zach [53] and shown in Fig. 9.8B. In Soeiro et al. [52], a two-channel parallel PWM interleaved DS-VSR implementing interphase transformers (IPTs) is proposed and experimentally verified, in which an asymmetric DPWM strategy is used owing to the advantages of semiconductor switching loss reduction. The implemented circuit and main experimental results for a 3.5-kW operation from a 127-V RMS grid and controlled DC-bus voltage of 380 V are shown in

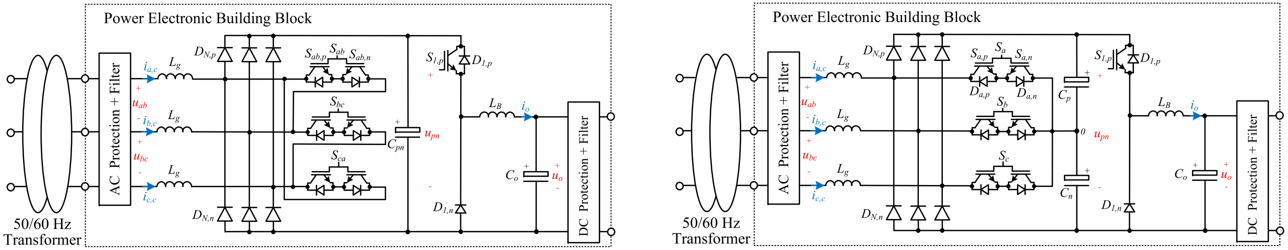

(a) (b)

FIGURE 9.8 Two-stage fast DC-type electric vehicle charger concept based on (A) Unidirectional two-level delta-switch rectifier; and (B) Three-level Vienna-type rectifier.

Fig. 9.9. A carrier-based PWM modulation employing a subset of $N = 2$ phase-shifted carriers displaced from each other within a pulse period by an angle of *2n/N* is used to multiply the number of voltage levels at the AC terminals. As shown in Fig. 9.9, line current feedback control is implemented in the $\alpha\beta$ coordinates, where variable $\alpha\beta$ components are obtained with the Clarke transformation. This control scheme includes an outer DC voltage loop that, together with information about the AC voltages in $\alpha\beta$, generates line current references $i_{\alpha,\beta}*$. A PLL circuit is used to determine instantaneous phase angle $\omega_g t$ from the grid line-to-line voltage measurements. This information identifies the voltage sextants for modulating the converter's active switches. Details about the modulation implementation can be found in Soeiro et al. [52].

Figs. 9.10 and 9.11 show typical two-stage high power DC-type charger infrastructures in which BESS and/or PV generation are incorporated into the circuit demanding a bidirectional front-end circuit. The power electronics topology in Fig. 9.10 implements the 2L-VSR circuit as the front-end, and Fig. 9.11 employs the three-level T-type VSR. A full SiC MOSFET-based 2L-VSR can achieve both high power efficiency and a compact design, as studied in Burkart and Kolar [54]. These performance metrics can be comparable to that attained with a full Si IGBT-based T-type VSR. A 5-kW hardware demonstrator of the SiC MOSFET-based 2L-VSR is shown in Fig. 9.12, together with the experimental results obtained at the rated power of the circuit connected to a 220-V RMS (phase-to-neutral) 50-Hz grid while controlling a DC-bus of 570 V and implementing SVPWM. A peak power efficiency of 99% and current total harmonic distortion (THD) of 2% are measured with the power analyzer Yokogawa WT500.

An 11-kW hardware demonstrator of an Si IGBT-based three-level T-type VSR is shown in Fig. 9.13, with the obtained experimental results at the rated power of the circuit connected to a 277-V RMS (phase-to-neutral) 50-Hz grid, while controlling a DC-bus of 680 V and implementing DPWM I. A peak power efficiency of 99% and current THD of 2.4% are measured with the power analyzer Yokogawa WT500.

Buck-type three-phase PFC rectifiers, also known as current source rectifiers (CSRs) [55–58], such as the one depicted in Fig. 9.14, are well-suited for EV battery charging systems because power conversion may be done in a single-stage (i.e., for AC public grid 380–480 V and battery voltage $u_o < 450$ V. The system enables a direct startup while naturally allowing for a dynamic current limitation. During startup, the two-stage circuits depicted in Figs. 9.8–9.11 require a precharging circuit for typical large DC-link capacitors, whereas CSRs can start up with the help of output inductor L by controlling the duty cycle of the active switches. Several other technologies of CSRs, which are suited for EV battery charging or DC distribution systems, are presented in Soeiro et al. [59].

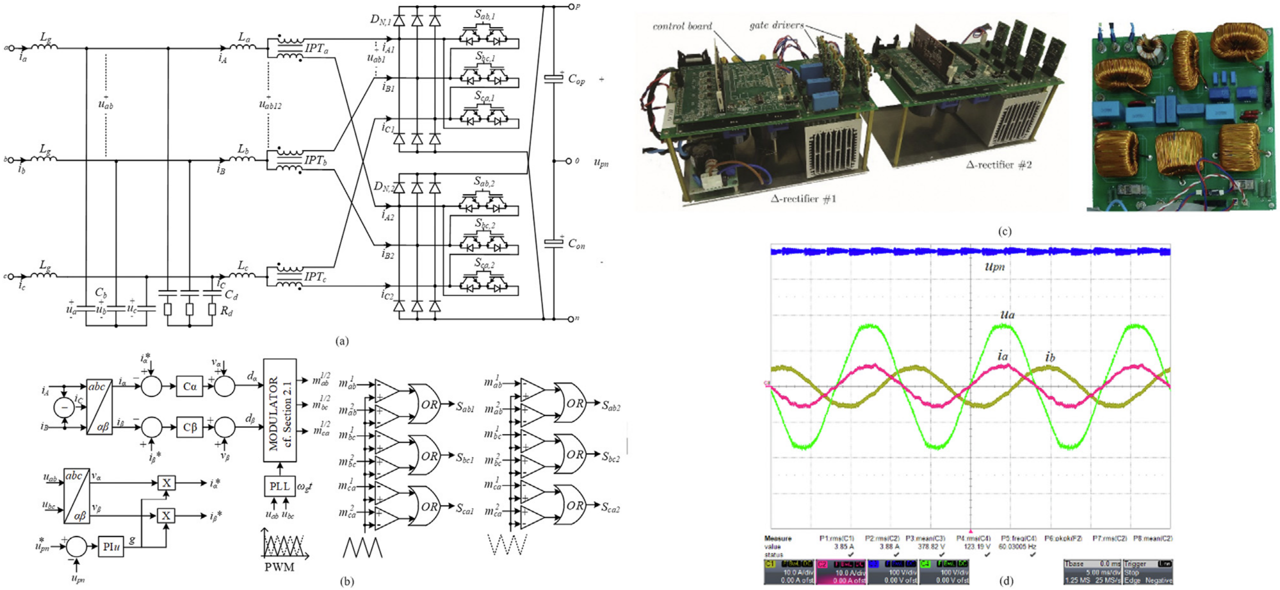

FIGURE 9.9 Three-phase two-channel delta-switch voltage source rectifier: (A) Circuit topology; (B) Feedback control strategy implementing symmetrically phase-shifted carrier based PWM modulation; (C) Hardware demonstrator; (D) main experimental waveforms. *IPT*, interphase transformer; *PLL*, phase locked loop.

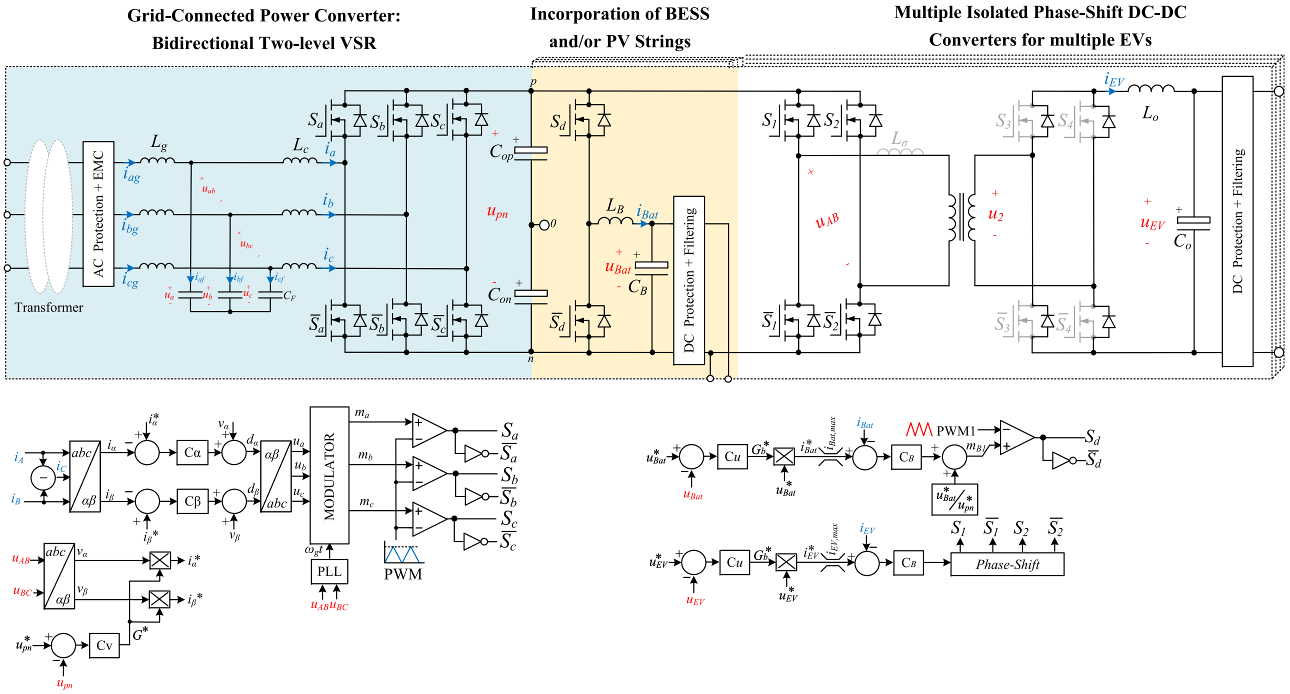

FIGURE 9.10 Typical high-power electric vehicle (EV) charging station and feedback control strategy implementing three-phase two-level voltage source rectifier (VSR) as front-end converter; a simple half-bridge converter as the battery energy storage system (BESS) dedicated charger; and multiple isolated phase-shift (forward-type) DC—DC converters for back-end charging of EVs. *PLL*, phase locked loop.

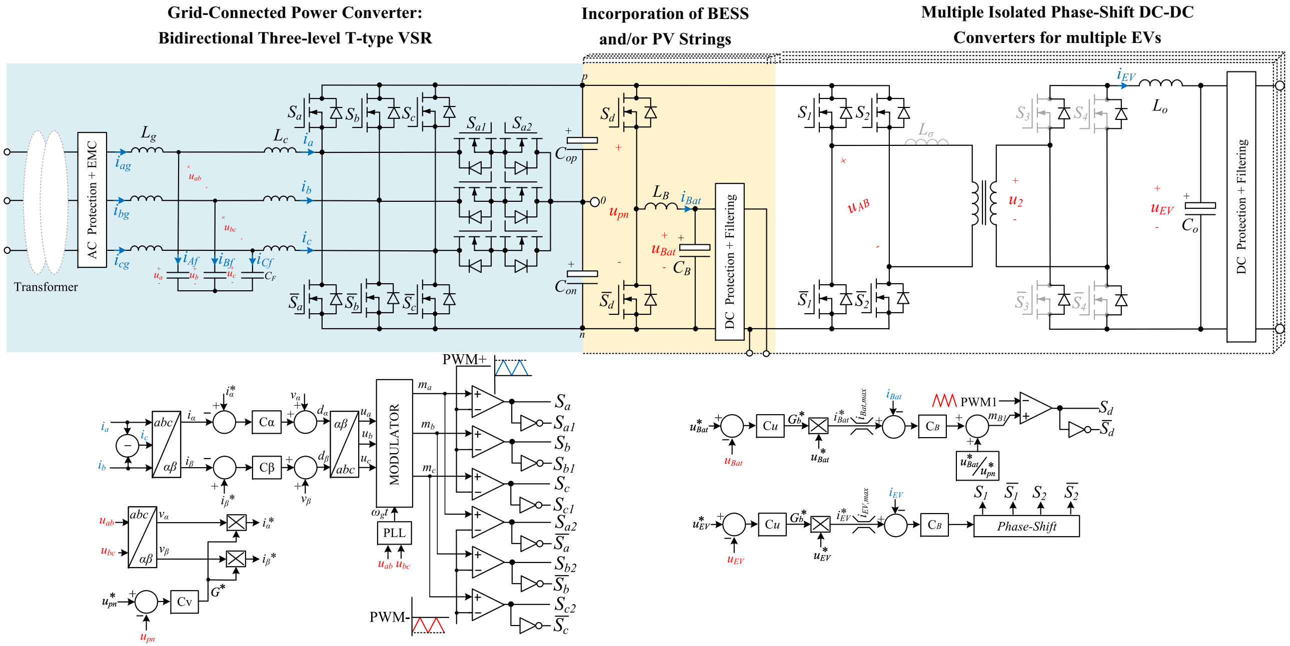

FIGURE 9.11 Typical high-power electric vehicle (EV) charging station and feedback control strategy implementing three-phase, three-level T-type voltage source rectifier (VSR) as front-end converter; a simple half-bridge converter as the battery energy storage system (BESS) dedicated charger; and multiple isolated phase-shift (forward-type) DC–DC converters for back-end charging of EVs. *PLL*, phase locked loop.

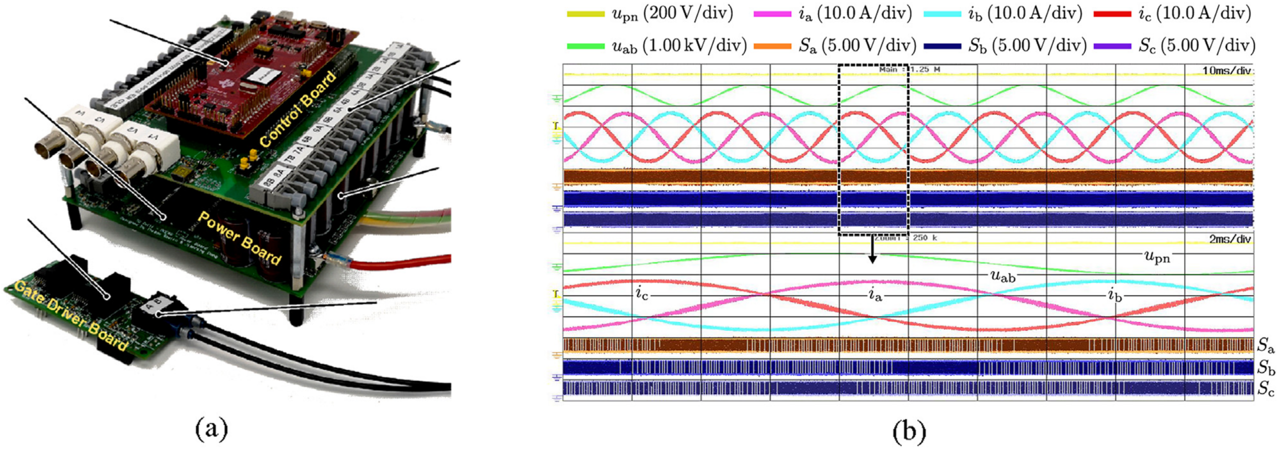

(a)

(b)

FIGURE 9.12 (A) Three-phase two-level voltage source rectifier 5-kW hardware demonstrator; (B) Main experimental results for SVPWM operation. Main variables shown are defined in Fig. 9.10.

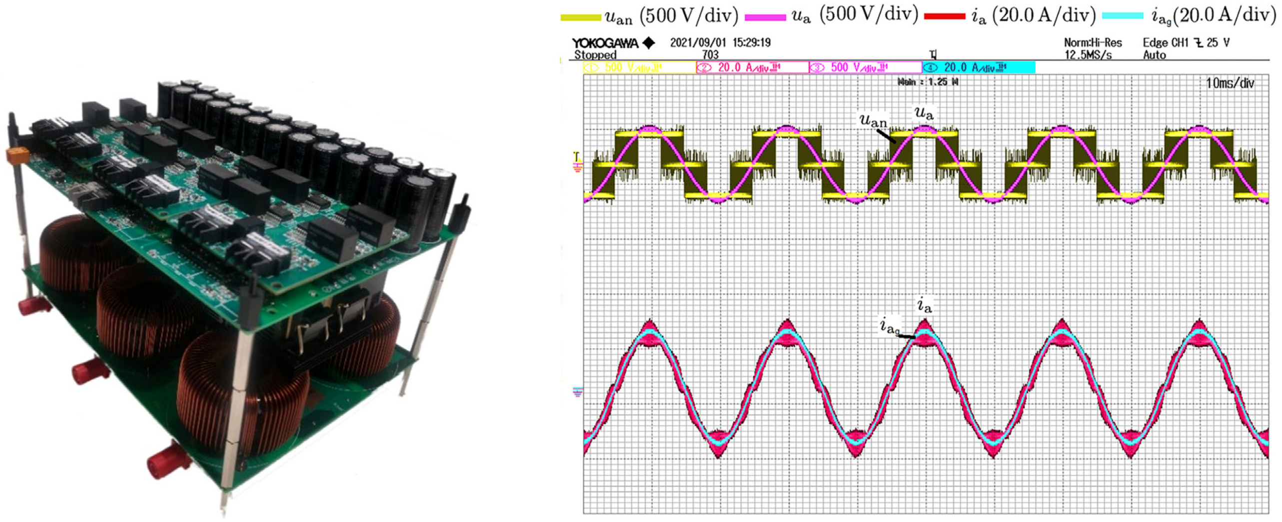

(a) (b)

FIGURE 9.13 (A) Three-phase, three-level T-type voltage source rectifier 11-kW hardware demonstrator; (B) Main experimental results for discontinuous PWM I operation. Main variables shown are defined in Fig. 9.11.

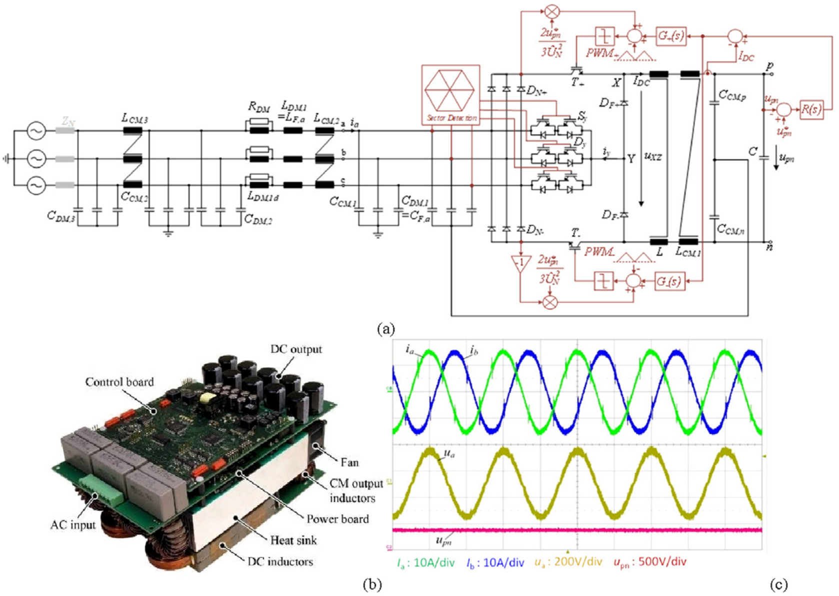

FIGURE 9.14 Swiss rectifier (A) Circuit schematic and feedback control strategy; (B) Hardware demonstrator; (C) Proof of concept. *CM*, common mode.

The CSR technology shown in Fig. 9.14, which was proposed in Soeiro et al. [55] and is known as the Swiss rectifier, can be fully controlled by the feedback voltage and current loops of the equivalent three-level buck-converter, defined by semiconductors $T_{+/-}$ and $D_{F+/-}$. As illustrated in the experimental results in Soeiro et al. [56], the circuit can deliver a current with low ripple to the EV battery while providing high−power factor operation. As described in Schrittwieser et al. [57], the Swiss rectifier can be seen as a two-stage conversion system in which the front end is composed of a low-frequency switched Vienna-type rectifier cascaded by a three-level buck-type converter. Therefore, higher efficiency is expected compared with the conventional two-stage circuit shown in Fig. 9.11. In Schrittwieser et al. [57], a 99.3% efficient circuit is designed and experimentally verified. For charging stations where multiple vehicles need to be charged, isolated DC−DC converters can be used to replace the equivalent three-level buck-type DC−DC converter. An exemplary implementation is shown in Fig. 9.15, where several phase-shift DC−DC converters are used to provide galvanic isolation between EV batteries and the grid.

In Manias and Ziogas [60], an interesting three-phase direct galvanic isolated AC-DC phase-shift forward-type converter was proposed. This circuit can implement ZVS turn-on in all switches by the appropriate use of their parasitic capacitances and transformer leakage inductance, L_{lkg}. This circuit,

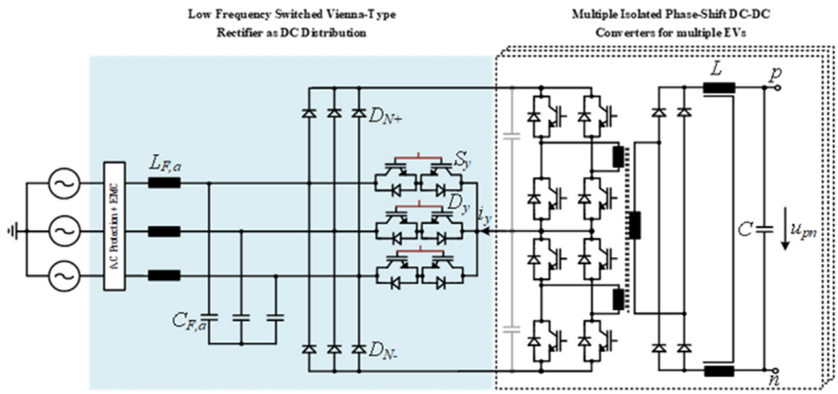

FIGURE 9.15 Swiss rectifier circuit adapted for multiple charging of electric vehicles (EVs) by implementation of multiple isolated DC−DC converters. *EMC*, electromagnetic compatibility.

which is depicted in Fig. 9.16, also benefits from low conduction loss (i.e., fewer semiconductors exist in the current path). In addition, considering that the boost-type PFC circuit depicted in Figs. 9.8−9.11 will most likely operate with hard-switching, during operation with high switching frequencies (i.e., $f_s > 8$ kHz), better performance in relation to switching losses can be expected for the direct AC−DC converter. Figs. 9.17 and 9.18 present the main AC- and DC-side voltage and current waveforms of a 50-kW direct AC−DC circuit obtained in a circuit simulator. The implemented feedback control and modulation strategy was proposed in Vlatkovic et al. [61]. As can be observed, the results demonstrate that the converter-side AC currents, i_a, i_b, and i_c, can effectively follow the sinusoidal 230-V RMS (phase-to-neutral) input phase voltages, u_a, b, c, whereas DC currents across the output inductors i_o and output voltage u_{pn} (400 V) are constant and well-regulated, attesting to the

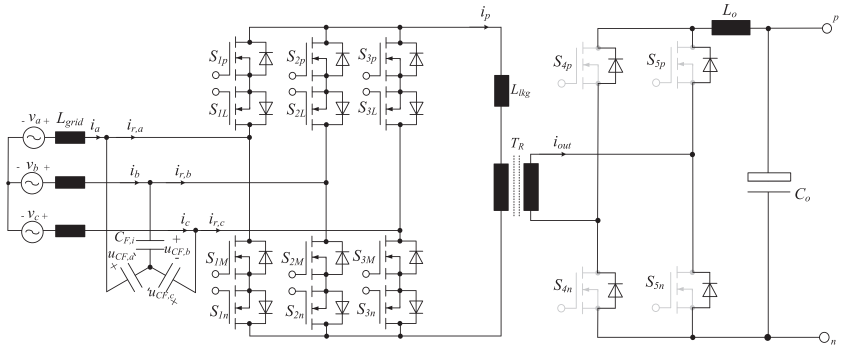

FIGURE 9.16 Three-phase galvanic isolated phase-shift forward-type direct AC−DC converter featuring zero voltage switching turn-on for all switches.

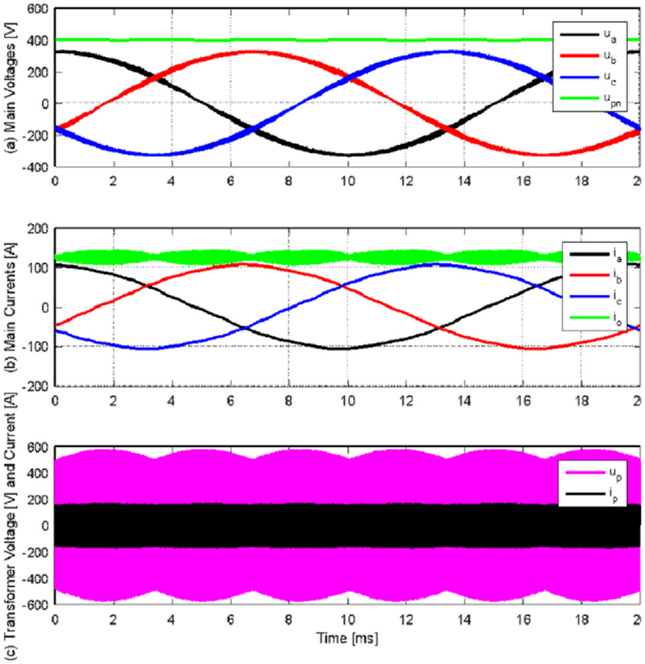

FIGURE 9.17 Main AC- and DC-side waveforms for direct isolated AC-DC phase-shift converter: (A) AC phase voltages u_{abc} and DC voltage u_{pn}; (B) AC phase currents i_{abc} and DC current i_o; (C) Full-bridge generated voltage u_p and transformer primary current i_p.

feasibility of the circuit. Fig. 9.18 shows a zoom on the transformer primary voltage and current, with all of the active switches' command states for grid sector I ($u_a > u_c > u_b$), where a ZVS turn-on of the switches can be observed.

9.4 Contactless charger

Contactless charging technology of EVs has undergone rapid development because it enables charging without galvanic contact and even dynamic charging in motion. Based on the operation principle, contactless charging can be classified into capacitive power transfer, in which the electric field is used to couple the transmitter (Tx) and the receiver (Rx); inductive power transfer (IPT), where the magnetic field is used for coupling; microwaves, and so on. Among them, IPT is more extensively used for EV charging because of its higher power rating and not high operating frequency.

Since 2015, several standards and regulations on IPT-based EV charging have been released and revised, including IEC 61980-1, SAE J2954, and ISO/PAS 19363:3017, in which the electromagnetic compatibility (EMC) limits, electromagnetic field exposure, operating frequency range, and transfer power

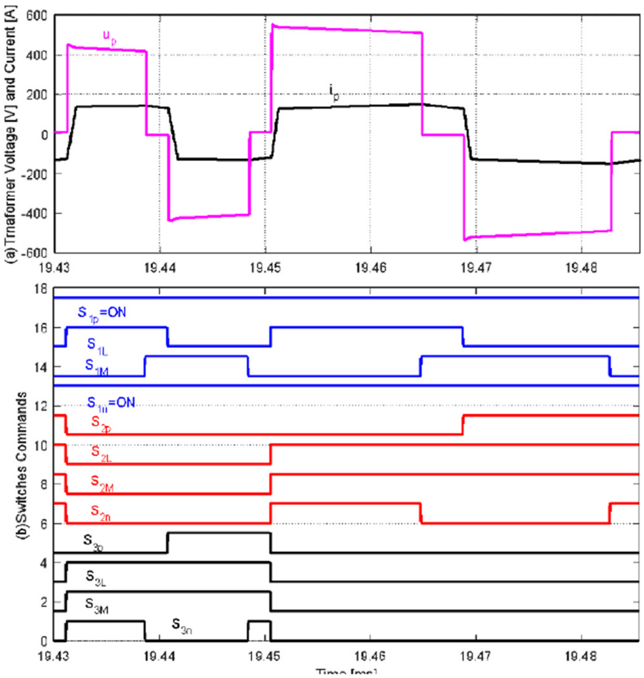

FIGURE 9.18 (A) Zoom on transformer applied voltage and current for grid sector I, where $u_a > u_c > u_b$; (B) Switches commands.

classes are specified. To date, they cover three power levels: 3.7, 7, and 11 kW, with a coil to ground clearance range of 100–250 mm and a nominal frequency of 85 kHz with a tuning band of 79–90 kHz [62]. Higher power levels (≥11 kW) have not yet been included in current regulations, but significant progress has been made on high-power IPT-based charging systems in research [63].

Fig. 9.19 presents the equivalent circuit of two coupled coils. By applying AC current i_1 to Tx coil L_1, induced voltage u_2 is generated in Rx coil L_2 according to Faraday's law. Depending on Rx side load voltage u_{ab}, AC

FIGURE 9.19 Circuit representation of coupled transmitting and receiving coils in typical inter-phase transformer systems.

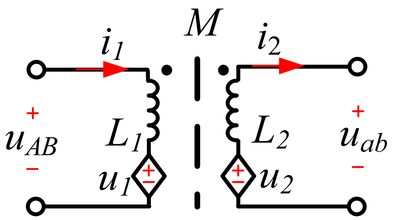

current i_2 through the Rx coil can be derived, which produces induced voltage u_2 in the Tx coil. The real power transferred through the magnetic coupling P_{12} is:

$$P_{12} = \omega M I_1 I_2 \sin \varphi_{12} \tag{9.1}$$

where ω is the operating angular frequency, M is the mutual inductance, φ_{12} is the phase difference between currents, and I_1 and I_2 are the rms value of the fundamental components of i_1 and i_2. The power losses are generally increased as higher I_1 and I_2 are applied. It is apparent that the efficiency can be increased by reducing I_1 and I_2. Moreover, ω, M, and $\sin\varphi_{12}$ must be increased for a fixed P_{12}, whereas certain design considerations must be respected, including the cost of components, the bandwidth of high-power semiconductors, and the allowed onboard construction volume. A higher operation frequency may imply higher eddy current losses in the coil and field shielding materials. To reduce the loss, finer strand Litz wire is required, leading to a higher cost and a larger outer diameter for the same effective cross-section.

The increase in M can be realized by putting the Tx and Rx coil closer, but it weakens flexibility. Another way is to apply more copper and ferrite to expand the size at a higher cost and lower power density. Because of the irregular geometry and nonlinearity of magnetic materials, the design of the coil usually relies on numerical methods. A trade-off emerges between the power density and efficiency, and a multiobjective optimization (MOO) design becomes necessary for the coil.

The value of $\sin\varphi_{12}$ peaks when φ_{12} is $\pi/2$, so the fundamental components of i_2 and u_2 are in phase. To achieve that, the input impedance seen from u_2 must be resistive, and thus a compensation is needed. Apart from improving the efficiency of the AC-link, the compensation can also enable the ZVS turn-on of the high-frequency inverter using MOSFETs as switches.

In the next subsections, the coil and compensation topologies of IPT-based EV charging systems will be reviewed. Then, an auto-resonant control method and a primary side model predictive control (MPC) method will be presented with experimental examples.

9.4.1 Coil topology

The magnetic coupler (Rx coil and Tx coil) is the core of the IPT system. Based on how coils are wound, the magnetic coupler can be classified into two types: (1) solenoid or double-sided flux couplers, in which magnetic flux is present on both sides of the coil; and (2) planar or single-sided flux couplers, in which charging coils have a planar shape, and magnetic flux is present only on one side of the coils. The latter can be further divided into two families based on the flux patterns: (1) unipolar couplers such as a single circular or rectangular coil; and (2) multicoil polarized couplers such as double D (DD) coils, bipolar pad, double D-quadrature (DDQ) coils, or three phase coils [64].

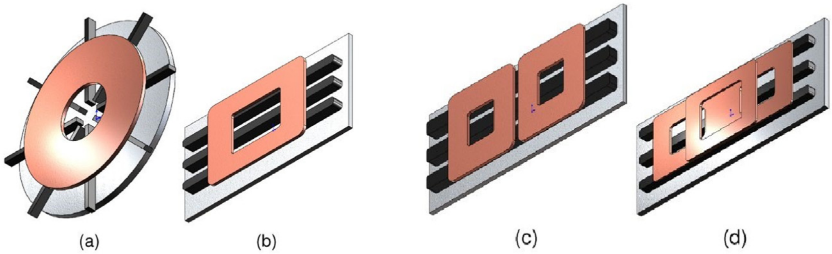

FIGURE 9.20 Mainstream single-sided flux magnetic couplers for interphase transformer system: (A) Circular; (B) Rectangular; (C) Double D; (D) Double D-quadrature [65].

Double-sided flux magnetic couplers are used less in practical IPT systems for EV charging because of relatively high flux leakage. Mainstream magnetic coupler topologies are shown in Fig. 9.20.

The performances of IPT systems, including the rated power, power transfer efficiency, power density, and misalignment tolerance, are limited by a number of design constraints. Because Rx-side components are mounted in the EV, the allowable space and weight of the circuit are bounded. A high power density of the IPT system is required. As mentioned, losses in the Litz wire and shielding have to be suppressed. Moreover, a large number of capacitors are used to deal with high voltage stresses. They result in conflicts between the power efficiency and power density of IPT systems. Another design constraint is the spatial offset between the Tx and Rx pads. It is required in the SAE J2954 standards for power efficiency from the grid connection to the output of the IPT system at misaligned conditions to be above 80%. To alleviate the drop in coupling, the size of charging pads should be increased, reducing the power density.

To achieve a trade-off among various design objectives including charging efficiency, power density, and stray field, numerical simulation-based MOO methods are often used to acquire a Pareto front for optimal magnetic coupler design. In Bandyopadhyay et al. [65], various loss mechanisms were studied and modeled. An MOO-based comprehensive comparison was carried out to compare four magnetic coupler topologies: circular Tx and Rx, rectangular Tx and Rx, DD Tx and Rx, and DD Tx with DDQ Tx [65]. Based on the MOO method, a 20-kW IPT system delivering 97.2% DC−DC system efficiency was built [66].

9.4.2 Compensation topology

Fig. 9.21 summarizes the compensation networks commonly used in EV wireless charging systems. The most straightforward method for compensation is to add capacitors to both sides in series or in parallel with Tx and Rx coils. Therefore, four basic compensation topologies are available: series−series

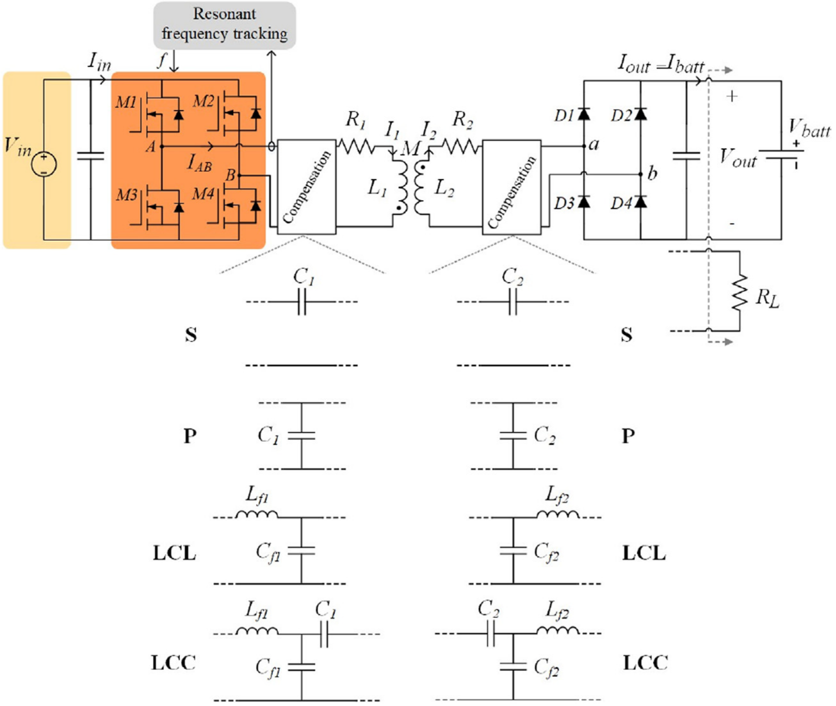

FIGURE 9.21 Schematics of typical interphase transformer systems for electric vehicle battery charging. Any combination of transmitter and receiver is possible. Here LCL and LCC represent inductor-capacitor-inductor and inductor-capacitor-capacitor respectively.

(SS), series—parallel, parallel—series (PS), and parallel—parallel. These four basic compensation topologies, as well as their design methods and ways to mitigate the bifurcation phenomenon (the presence of multiple resonant frequencies), are studied in Chopra and Bauer [67].

Among the four basic compensation topologies, SS compensation has advantages over other topologies. For SS, the choice of compensation capacitances on both sides is independent of either load or mutual inductance between Tx and Rx. In addition, the output current from the SS compensation is load-independent (i.e., it has a current-source characteristic). This property makes SS compensation suitable for directly charging lithium-ion batteries, which work as a voltage source. However, the input impedance of the SS-compensated system drops with the coupling coefficient or as the load resistance increases. Thus, if the two coils are not perfectly aligned, or when the secondary coil is absent, it may lead to overcurrent problems. This requires soft starting and shutdown strategies and leads to limited misalignment tolerance. Moreover, voltage stress on the compensation component is high because only one bears the voltage at each side of the SS compensation.

High-order compensation systems using multiple L (inductor) or C (capacitor) elements can be employed to overcome the limits of basic compensation topologies. For example, P compensation has a voltage source characteristic. Therefore, it is impossible to connect it directly with the commonly used voltage-source inverter or a battery, which would require a current-source supply or load. To overcome the need for large DC inductors, compensation L has been employed in high-frequency circuits such that the P compensation capacitor can be interfaced with voltage-source converters. This has resulted in T-type compensation networks such as LCL and LCC. Essentially, these compensations are tuned so that both passive components connected at the right and left of the T circuit are in resonance with the parallel capacitor. Among them, double-sided LCC compensation has high resiliency to load and coupling coefficient variations [68]. LCC-S compensation realizes stable output under high misalignment and has high tolerance to both short and open circuit faults at the load side, which is critical for safe operation [69].

In reality, the components' tolerance and degradation owing to the rise in use and temperature can affect the resonance of the IPT system. Variable compensation networks have been used to counteract this detuning and enhance power transfer efficiency, such as switch-controlled capacitors, which were introduced to regulate resonant converters in Gu and Harada [70]. Besides resonance tuning, variable compensation components can have an active role in the common control strategy of load matching for maximal efficient operation, as explained in Zhang and Mi [63]. Variable compensation based on switching capacitors or inductors is able to make the optimum load condition invariant of the coupling coefficient, which eliminates the need for a DC−DC converter at the load side [71].

9.4.3 Soft-switching operation and resonant frequency tracking

In practice, the compensation network is rarely tuned to operate at an exact resonance. For example, Feng et al. [72] showed that an SS compensation with the primary side inductively tuned and secondary side capacitively tuned is less sensitive to coupling variations than the fully tuned system (i.e., is more resilient to misalignment).

Usually, small detuning from the resonance is desirable in any compensation network to achieve the ZVS turn-on of the high-frequency inverter, as shown in Fig. 9.22. As explained in Grazian et al. [73], ZVS turn-on is realized when Z_{in} is inductive, so current i_{AB} must be lagging inverted voltage v_{AB}, as illustrated in Fig. 9.23. As a consequence, all MOSFETs must be switched off before the current crosses zero. During the dead time, the remaining current would flow through the antiparallel diodes of the MOSFETs. This turnoff current level has to be enough to discharge the drain-source capacitance of those MOSFETs before that they are turned on and start conducting. Moreover, it is not preferable to set the operation too deeply into the inductive

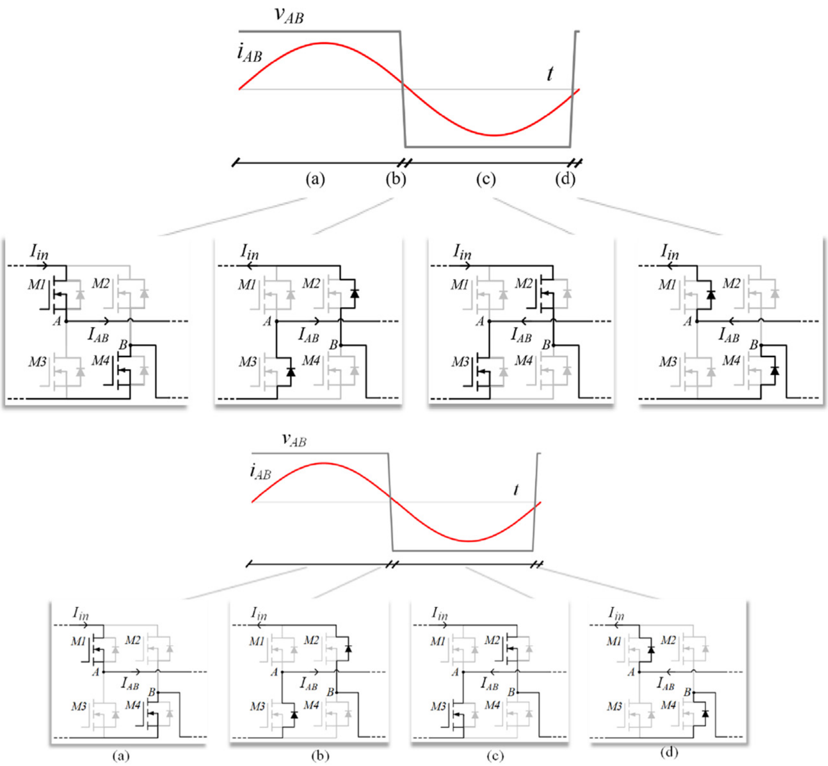

FIGURE 9.22 Inverted voltage v_{AB} and current i_{AB} ensure the zero voltage switching turn-on operation of the primary inverter. (A) MOSFETs M1 and M4 conduct the positive half-wave of i_{AB}. (B) M1 and M4 are turned off when the current is still positive. During the dead time, current flows through the antiparallel diodes of M2 and M3 that discharge their drain-source capacitance before they start conducting. (C, D) Operation of M2 and M3, which is equivalent to the previous half-period in (A, B).

region of the resonant circuit because this would increase the turn-off losses and eventually worsen power transfer efficiency owing to low power factor. Therefore, an optimized turn-off instant must be found.

To guarantee an optimized ZVS turn-on operation at any magnetic coupling and load condition, it is essential to implement feedback control for the inverter. The most common strategy consists of detecting the zero-crossing of the current i_{AB} and switching the inverter bridge before that instant. This detection can be realized by employing differential comparators. These compare the measured current with detection referenced tuned at the optimized current level. However, these references must also account for the delay introduced by the feedback control. Zhou et al. [14] demonstrated analytically and experimentally that this delay depends on the slope of the current around its zero-crossing. Considering that the coupling coefficient is not constant and

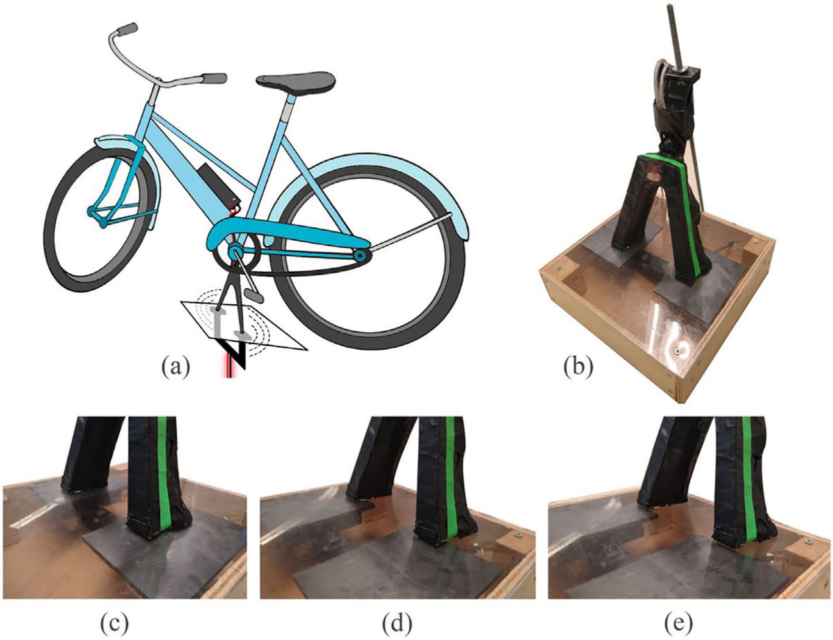

FIGURE 9.23 Magnetic coils of 200-W electric bike (e-bike) wireless charging system used to prove autoresonant control: (A) Illustration of e-bike; (B) Overview of aligned coils. Coils' alignment for: (C) $k = 0.266$; (D) $k = 0.201$; (E) $k = 0.147$ [74].

the load varies during the charging cycle, the amplitude and the frequency of the current i_{AB} are not fixed, so the feedback control needs variable voltage references to the comparators to detect the optimized ZVS turn-on point. This concept is termed auto-resonant control and was demonstrated in a laboratory prototype of a 200 W electric bike (e-bike) wireless charging system, the magnetics components of which are shown in Fig. 9.24. Measured waveforms at different coupling coefficients are shown in Fig. 9.25, where it is clear that the variable detection references led to the ZVS turn-on of the inverter during startup.

9.4.4 Power flow and model predictive control of interphase transformer systems

Fig. 9.26 shows the core system topology of an IPT-based contactless charging system. The primary-side DC−AC converter, primary compensation, magnetic Tx and Rx, secondary compensation, and secondary rectifier form a resonant converter. On the primary side, the AC−DC converter is placed between the grid and the resonant converter for power factor correction (PFC). An optional DC−DC converter can also be placed between the primary AC−DC converter

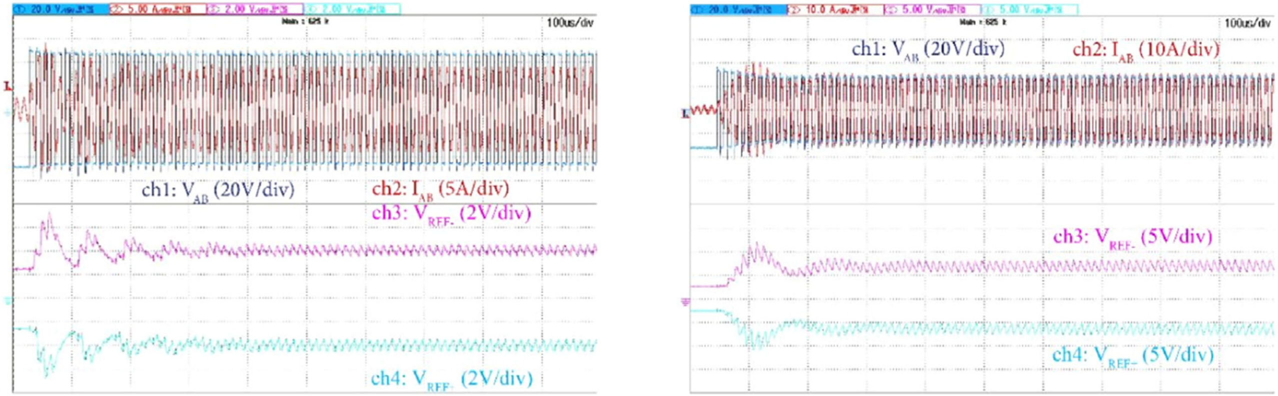

(a) (b)

FIGURE 9.24 Measured inverted voltage V_{AB}, current I_{AB}, and references $\mathrm{V}_{\mathrm{REF}+}$, $\mathrm{V}_{\mathrm{REF}-}$ for the detection of the positive and negative slope of I_{AB}. These result from the autoresonant control measured at: (A) $k = 0.266$; (B) $k = 0.147$, which correspond to the coil's alignments in Fig. 9.22C and D, respectively [74].

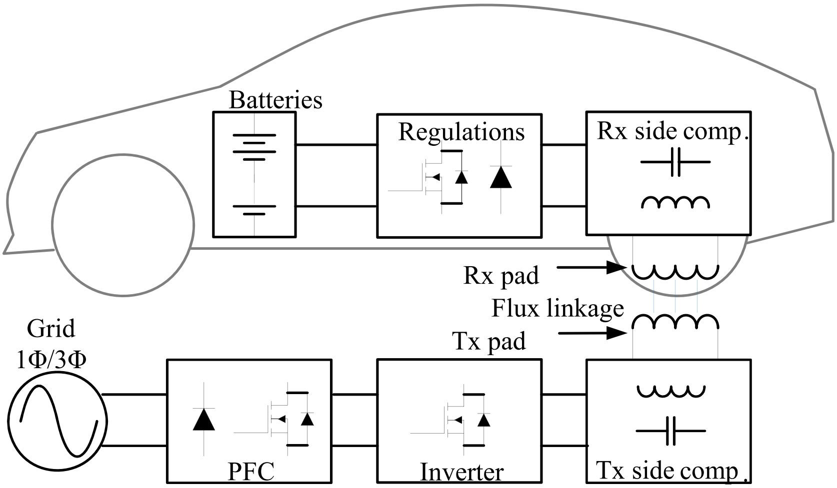

FIGURE 9.25 Schematics of core structure of inductive power transfer–based contactless charging system for electric vehicle including a power factor correction (PFC) as the front end. *Rx*, receiver; *Tx*, transmitter.

and the DC–AC converter for power and voltage regulation. Similarly, on the secondary side, an optional DC–DC converter can be placed between the batteries and the rectifier for the same purposes.

As mentioned, the IPT system is sensitive to the coupling coefficient, operation frequency, and load variations. Control is necessary to have safe transient behavior, especially during startup and shutdown, and to regulate power flow efficiently for battery charging [75]. Depending on the system topology and choice of control variables, the power flow control methods can be classified into three categories: primary-side control, secondary-side control, and dual-side control.

Primary-side control regulates power flow by controlling current through the primary coil, which can be achieved by phase shifting the primary-side inverter, adding a front-end DC–DC converter to vary the DC bus voltage, or changing the switching frequency from the resonant frequency. The required voltage and current from the secondary side should be transferred to the primary side via wireless communication [13].

Secondary-side control uses an active rectifier or an additional DC–DC converter to regulate the charging current. In Zhou et al. [14], secondary-side MPC is implemented with a back-end buck converter to ensure reliable power flow control when the coupling coefficient is rapidly changing, which is suitable for a dynamic charging application.

In dual-side control, the primary-side converter and secondary-side converter are controlled at the same time. This requires low latency and highly reliable wireless communication between the sides, but it also brings flexibility

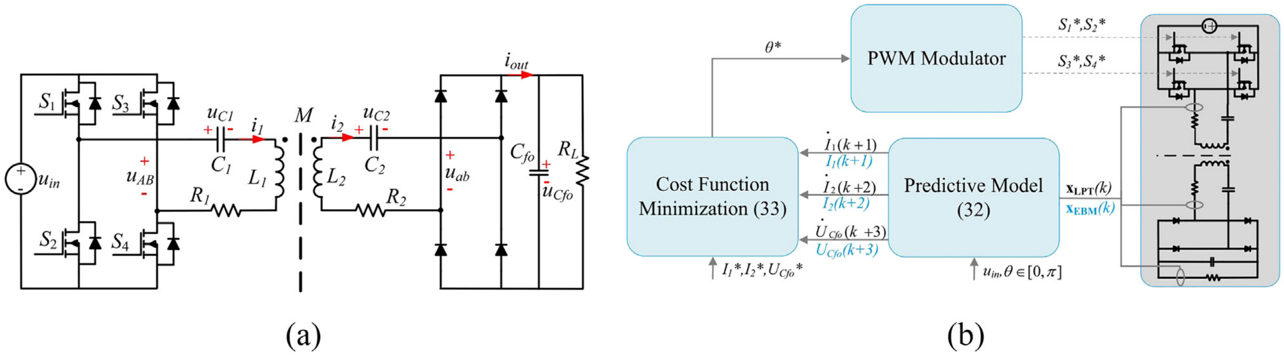

FIGURE 9.26 Model predictive control (MPC) control of the series−series compensated interphase transformer (IPT) system: (A) Schematic of the studied IPT system; (B) MPC controller diagram.

and advantages, For example, optimal load matching can be achieved by the Rx side DC–DC converter, whereas output voltage regulation can be realized by the Tx side converter. In Diekhans and De Doncker [15], dual-side control is implemented using active H-bridges on both sides only, without involving DC–DC converters. Front-end and back-end DC–DC converters can also be adopted for dual-side control [76]. In this case, the H-bridge converters operate at a constant switching frequency and duty cycle, and their switching losses can be minimized.

A primary side model predictive controller based on a reduced-order dynamic model of the IPT system was proposed in Shi et al. [77]. The core schematic of an SS-compensated IPT system is depicted in Fig. 9.26A. Output voltage u_{Cfo} can be regulated by adjusting phase angle θ between the gate signals of each diagonal pairs of the switches (S1–S4 or S3–S2) [78]. Provided the system is operating near the resonance and the magnetic coupling is low, a reduced-order state-space model of the S–S compensated IPT system is as described in Shi et al. [77]:

$$\begin{bmatrix} I_1' \\ I_2' \\ U_{Cfo}' \end{bmatrix} = A \begin{bmatrix} I_1 \\ I_2 \\ U_{Cfo} \end{bmatrix} + B\sin\frac{\theta}{2}, A = \begin{bmatrix} -\frac{R_1}{2L_1} & -\frac{\omega_s M\cos\alpha_2}{2L_1} & 0 \\ \frac{\omega_s M\cos\alpha_2}{2L_2} & -\frac{R_2}{2L_2} & -\frac{2}{\pi L_2} \\ 0 & \frac{2}{\pi C_{fo}} & -\frac{1}{C_{fo}R_L} \end{bmatrix},$$

$$B = \begin{bmatrix} \frac{2U_{in}\cos\alpha_1}{\pi L_1} \\ 0 \\ 0 \end{bmatrix} \tag{9.2}$$

where U_{in} and U_{Cfo} are the average value of u_{in} and u_{Cfo}, I_1 and I_2 are the amplitude of the fundamental component of i_1 and i_2. α_1 represents the phase angle of the waveform of i_1 in relation to u_{ab}. α_2 denotes the phase angle between i_2 and the Rx coil-induced voltage. The MPC applies the system analytical model to predict the future behavior of a system periodically, which is insensitive to disturbances and can provide a fast dynamic response. The discrete predictive model can be expressed as:

$$x(k+1) = (T_sA + I_{3\times3})x(k) + T_sB\sin\frac{\theta}{2}, \text{ where } x(k) = \left[I_1(k), I_2(k), U_{Cfo}(k)\right]^T \tag{9.3}$$

where T_s is the switching period. Based on Eq. (9.3), the MPC controller is

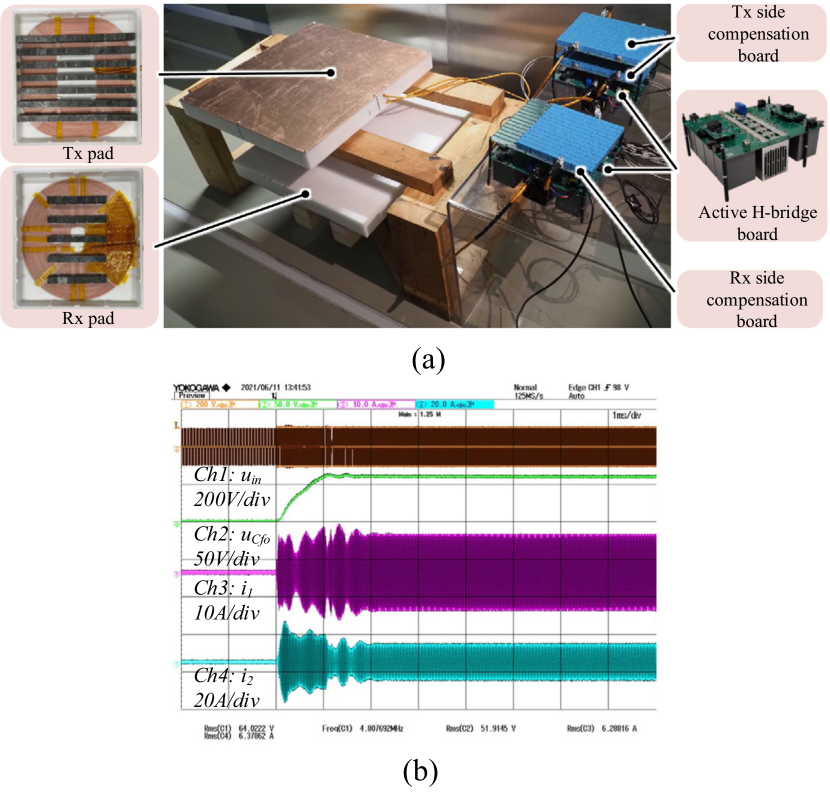

(a)

(b)

FIGURE 9.27 Experimental setup and startup response: (A) 20-kW interphase transformer prototype; (B) Startup response using proposed model predictive controller. *Rx*, receiver; *Tx*, transmitter.

designed as shown in Fig. 9.26B. The developed MPC controller is applied on the IPT system presented in Fig. 9.27A, where an active full-bridge converter is adopted as the synchronous rectification stage. The experimental results are illustrated in Fig. 9.27B, where u_{Cfo} reaches the steady state in 1.5 ms with almost no overshoot.

9.5 Power quality of EV charging

9.5.1 Power quality parameters and grid codes

Grid-connected devices rely on the compatibility level promised by the grid operator. These devices also influence the compatibility of the grid. In this context, the concept of PQ is established, which defines grid compatibility in a broad set of aspects of the grid voltage and the emissions of the devices. Table 9.3 lists PQ parameters and their description [79].

TABLE 9.3 Power quality parameters and their descriptions [79].

Power quality parameters		Description
Voltage sag		Undervoltage exceeding threshold (e.g., 90% of nominal grid voltage)
Voltage swell		Overvoltage exceeding threshold (e.g., 110% of nominal grid voltage)
Voltage imbalance		RMS values of line or phase voltages are not equal
Voltage fluctuation	Rapid voltage change	Quick transition in RMS voltage between two steady-state conditions
	Flicker	Fluctuation of grid voltage's RMS value leading to unsteadiness of light stimulus
Voltage interruption		Reduction in grid voltage below interruption threshold (e.g., 10% of nominal grid voltage)
Frequency deviation		Measured frequency is different from nominal one
Voltage deviation		Measured voltage is different from nominal one
Nonfundamental distortion		Distortion of grid voltage or current induced by nonfundamental components

Worldwide, different PQ standards are adopted in different areas. The most commonly adopted two sets of PQ standards are IEEE PQ standards and IEC 61000 series. Table 9.4 lists the IEEE and IEC standards and PQ parameters covered by them. A more detailed comparison of the two standards is presented in Wang et al. [1].

Battery chargers are essentially grid-connected power electronic converters made of switching components, which are nonlinear loads. Hence, battery chargers may lead to the noncompliance of nonfundamental distortion (i.e., harmonics, interharmonics, and supraharmonics), which have been found in the other power electronics-based applications such as wind farms and PV farms [80,81]. In addition, for high-power chargers, a high $\frac{dp}{dt}$ during the startup transient may result in a voltage fluctuation noncompliance, especially under a high grid impedance condition. Therefore, potential PQ issues, such as the noncompliance of nonfundamental distortion and voltage fluctuation, brought by battery chargers are expected. The following section introduces factors (e.g., the charger's design and grid impedance) that influence the PQ performance of EV chargers.

9.5.2 Voltage fluctuation

The voltage fluctuation refers to the RMS voltage variation within a certain threshold (e.g., ±10% of the nominal voltage), in the short term. To analyze

TABLE 9.4 Overview of IEEE and IEC power quality standards.

	Medium-voltage			Low-voltage (≤1 kV)		
	IEEE (1–69 kV)	IEC (1–35 kV)		IEEE	IEC	
		Compatibility level	Emissions and planning level		Compatibility level	Emissions and planning level
Voltage level	1159	61000-2-4	N.A.	1159	6000-2-4	N.A.
Voltage fluctuation	1453	61000-2-12	61000-3-7	1453	61000-2-2	61000-3-5
Voltage imbalance	N.A.	61000-2-12	61000-3-13	141	61000-2-2	61000-3-14
Current distortion	519	N.A.	61000-3-6	519	N.A.	61000-3-4, 61000-3-14
Voltage distortion	519	61000-2-12	61000-3-6	519	61000-2-2	61000-3-14

N.A., not available.

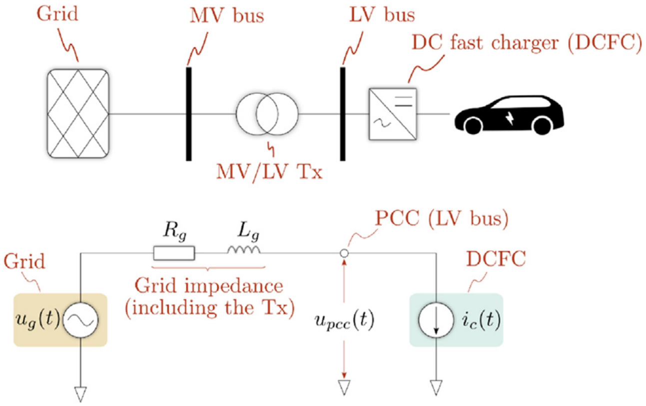

FIGURE 9.28 Simplified model of grid-charger system for flicker severity analysis. *DCFC*, direct current fast charger; *LV*, low-voltage; *MV*, medium-voltage; *Tx*, transmitter.

the voltage fluctuation induced by EV charging, the simplified model illustrated in Fig. 9.28 is generally used. In this model, the grid is simplified as a voltage source and grid impedance. The voltage of the point of common coupling (PCC), U_{PCC}, is given by:

$$U_{PCC}(t) = U_g(t) - Ri(t) - L\frac{d}{dt}i(t) \tag{9.4}$$

where R is the resistance of grid impedance, L is the inductance of grid impedance, U_g is the grid voltage, and i is the input current of the direct current fast charger (DCFC). Because the DCFC's input current, or load current, is determined by the charging power, i.e., $P(t) = U_{PCC}(t)i(t)$, Eq. (9.4) can be rewritten as:

$$\frac{d}{dt}U_{PCC}(t) = \frac{{U_{PCC}}^3(t) - {U_{PCC}}^2(t)U_g(t) + RU_{PCC}(t)P(t) + LU_{PCC}(t)\frac{d}{dt}P(t)}{LP(t)} \tag{9.5}$$

Therefore, the fluctuation of $U_{PCC}(t)$, or $\frac{d}{dt}U_{PCC}(t)$, is influenced by the charging power and its derivative, the grid impedance magnitude, the grid impedance angle, the grid voltage level, and the PCC voltage level.

9.5.3 Nonfundamental distortion

The nonfundamental distortions of grid current and voltage are categorized as the harmonic, interharmonic, and supraharmonic distortions according to the frequency (f_d) of the nonfundamental components. If f_d is the integer multiple of the fundamental frequency and is below 2 kHz, the component is called harmonic. On the contrary, if f_d is the noninteger multiple of the fundamental frequency and is below 2 kHz, the component is called interharmonic. Supraharmonic refers to the nonfundamental component whose frequency is higher than 2 kHz but lower than 150 kHz [82]. The component with a frequency higher than 150 kHz is called EMI.

To analyze the nonfundamental distortion emissions of chargers and the other power electronics–based applications, an effective method is the impedance-based modeling method [83]. The impedance model of a grid-charger system is a small-signal model, which is illustrated in Fig. 9.29. As shown, the grid is simplified as background voltage source V_g and grid impedance Z_g at the PCC of the charger. On the other hand, the charger is simplified as nonfundamental current source I_c and input impedance Z_c. Here, the charger is simplified as the Norton equivalent circuit instead of the Thevenin equivalent circuit because the input current of the charger is controlled. According to the impedance model, the nonfundamental current emission (I_e) of the charger can be calculated as [34]:

$$I_e(s) = \frac{Z_c(s)}{Z_c(s) + Z_g(s)} I_c(s) - \frac{1}{Z_c(s) + Z_g(s)} V_g(s) \tag{9.6}$$

The nonfundamental current emission of the charger is also influenced by the nonfundamental background voltage. Moreover, if the nonfundamental current emission of the charger meets the requirement of the grid codes under ideal grid conditions, it only guarantees the compliance of I_c. When the grid is nonideal (i.e., Z_g is not zero), I_c can be amplified if there is resonance between Z_c and Z_g, which may result in noncompliance. In the worst case, the real part of Z_c is negative at some frequencies owing to the poorly tuned control parameters, which leads to system instability [34,84].

To ensure the stability of the grid-charger system and nonfundamental current emission compliance of the charger, commonly adopted measures include:

- Reducing I_c by increasing switching the frequency, increasing the inductance of the power filter, and so on,

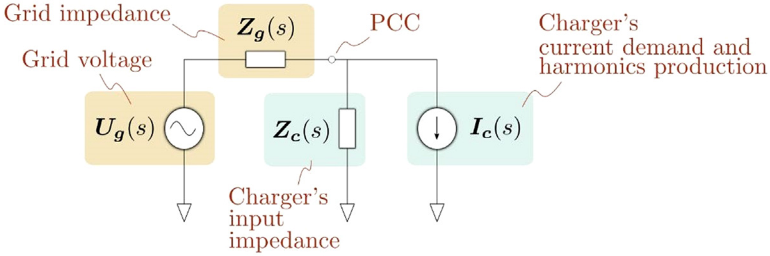

FIGURE 9.29 Impedance model of charger-grid system.

- Preventing the negative resistance of Z_c by carefully designing the control of the charger,
- Increasing the magnitude of Z_c at frequencies at which nonfundamental components exist in the V_g (e.g., adding a PR (proportional resonant) compensator at those frequencies in the current controller), and
- Preventing resonance between Z_c and Z_g at frequencies where nonfundamental components exist in I_c and V_g.

Because EV chargers need to pass the grid compliance test in the production test, the I_c is normally not problematic. However, the grid impedance Z_g at the PCC to which chargers are connected varies quite a lot from one case to another, which brings lots of challenges for designing the chargers. Moreover, grid conditions are time-variant. In this context, compliance of nonfundamental distortion emissions of the charger are hard to ensure with a fixed design.

To explain how the charger's Z_c is influenced by the design, a case study on a typical offboard charger is presented. As introduced in Wang et al. [1] and Rivera et al. [85], an offboard charger is normally composed of several power modules with a lower power rating. Inside the power module, there is an AC—DC converter and a DC—DC converter. The nonfundamental emission of the charger is mainly influenced by the AC—DC converter because the DC—DC converter is greatly decoupled by the DC-link capacitor. The typical topology used for the AC—DC converter in the power module includes the two-level active front end (AFE) and the Vienna rectifier. For simplicity, the Vienna rectifier was selected for this case study. However, the method presented here is also applicable to the two-level AFE, because the average model of the Vienna rectifier is the same as that of the two-level AFE [86].

Fig. 9.30 shows a typical design of the AC—DC converter of an offboard charger. Here, a PI (proportional integral) controller in the synchronous rotational frame is used for the current controller, whereas the synchronous rotational frame phase lock loop (SRF-PLL) is used for the grid synchronization.

For the next step, the impedance model of the rectifier will be derived. To start with, the average model of the rectifier in the αβ-frame is given by Eq. (9.7):

$$\begin{cases} V_{s\alpha} = Lsi_{s\alpha} + Ri_{s\alpha} + \dfrac{V_{dc}}{2}d_{s\alpha} \\ V_{s\beta} = Lsi_{s\beta} + Ri_{s\beta} + \dfrac{V_{dc}}{2}d_{s\beta} \end{cases} \tag{9.7}$$

where $V_{s\alpha}$ and $V_{s\beta}$ are the α-axis and β-axis component of the grid voltage, respectively; $i_{s\alpha}$ and $i_{s\beta}$ are the α-axis and β-axis components of the input

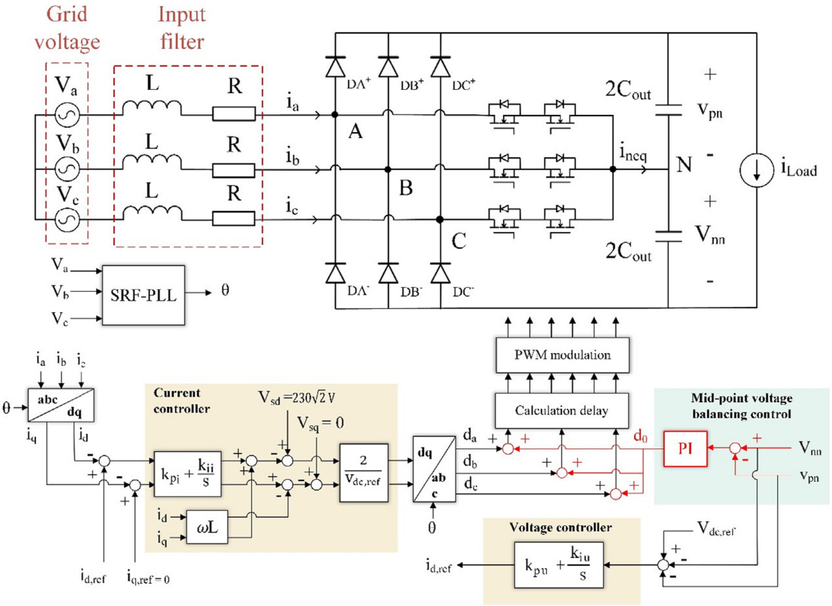

FIGURE 9.30 Typical circuit and control of AC—DC converter in power module of offboard charger. *SRF-PLL*, synchronous rotational frame phase lock loop.

current, respectively; and $d_{s\alpha}$ and $d_{s\beta}$ are the α-axis and β-axis component of the duty cycle. Here, the DC-link voltage dynamics is ignored because of the large capacitance of the DC-link capacitor, which is generally accepted in existing impedance models [87]. Because of the use of a digital control, there is a total delay of 1.5 switching cycle T_{sw} [88]. As a result, the block diagram of the average model of the Vienna rectifier with the control loop is depicted in Fig. 9.4. The transfer matrices $\boldsymbol{H_i(s)}$, $\boldsymbol{G_{del}(s)}$, and $\boldsymbol{Y(s)}$ are given in Table 9.5 and Fig. 9.31.

TABLE 9.5 Transfer function blocks in Fig. 9.3

	$H_i(s)$	$G_{del}(s)$	$Y(s)$
Transfer function	$\begin{bmatrix} k_{pi}+\frac{k_{ii}}{s} & 0 \\ 0 & k_{pi}+\frac{k_{ii}}{s} \end{bmatrix}$	$\begin{bmatrix} e^{-1.5T_{sw}s} & 0 \\ 0 & e^{-1.5T_{sw}s} \end{bmatrix}$	$\begin{bmatrix} Ls+R & 0 \\ 0 & Ls+R \end{bmatrix}^{-1}$

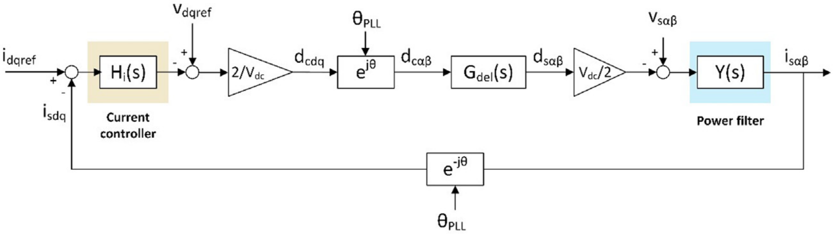

FIGURE 9.31 Block diagram of average model of Vienna rectifier including the control loop. The DC-link voltage dynamics and voltage control loop are ignored. *PLL*, phase locked loop.

The average model can be linearized if the charger operates at a steady state. Assuming $\boldsymbol{\theta_{PLL}} = \boldsymbol{\theta_1} + \boldsymbol{\Delta\theta}$, where $\boldsymbol{\theta_1}$ is the phase angle of the grid voltage, the transform matrix $\boldsymbol{e^{j\theta_{PLL}}}$ can be rewritten as $\boldsymbol{e^{j\theta_1}e^{j\Delta\theta}}$. Besides, assuming $\boldsymbol{\theta_1} = \boldsymbol{\omega_1 t}$, the following transform [13] exists:

$$\boldsymbol{e^{-j\omega_1 t}G_{del}(s)e^{j\omega_1 t}} = \boldsymbol{G_{del}(s+j\omega_1)} = \begin{bmatrix} \cos(\omega_1 T_{del})e^{-T_{del}s} & \sin(\omega_1 T_{del})e^{-T_{del}s} \\ -\sin(\omega_1 T_{del})e^{-T_{del}s} & \cos(\omega_1 T_{del})e^{-T_{del}s} \end{bmatrix} \tag{9.8}$$

$$\boldsymbol{e^{-j\omega_1 t}Y(s)e^{j\omega_1 t}} = \boldsymbol{Y(s+j\omega_1)} = \begin{bmatrix} Ls+R & -L\omega_1 \\ L\omega_1 & Ls+R \end{bmatrix}^{-1} \tag{9.9}$$

With the transform given by Eqs. (9.8) and (9.9), the whole system can be transformed into the synchronous dq-frame. Furthermore, because $\boldsymbol{\Delta\theta}$ is small, the transform matrix $\boldsymbol{e^{j\Delta\theta}}$ can be linearized, as expressed by Eq. (9.10):

$$\boldsymbol{e^{j\Delta\theta}} = \begin{bmatrix} \cos(\Delta\theta) & \sin(-\Delta\theta) \\ \sin(\Delta\theta) & \cos(\Delta\theta) \end{bmatrix} \approx \begin{bmatrix} 1 & -\Delta\theta \\ \Delta\theta & 1 \end{bmatrix} = \boldsymbol{I} + \boldsymbol{J}\Delta\theta \tag{9.10}$$

where $\boldsymbol{I} = \begin{bmatrix} \mathbf{1} & \mathbf{0} \\ \mathbf{0} & \mathbf{1} \end{bmatrix}$ and $\boldsymbol{J} = \begin{bmatrix} \mathbf{0} & \mathbf{-1} \\ \mathbf{1} & \mathbf{0} \end{bmatrix}$. Besides, when transforming certain variables with the transform matrix $\boldsymbol{e^{j\Delta\theta}}$, the product of two small signals can be neglected. For instance, the simplification for transforming $\boldsymbol{d_{cdq}}$ with $\boldsymbol{e^{j\Delta\theta}}$ is given by Eq. (9.11), where $\boldsymbol{D_{cd}}$ and $\boldsymbol{D_{cq}}$ are the duty cycle in steady state and $\boldsymbol{\widetilde{d_{cd}}}$ and $\boldsymbol{\widetilde{d_{cq}}}$ are the small signal in the duty cycle. Because $\boldsymbol{\Delta\theta}$, $\boldsymbol{\widetilde{d_{cd}}}$, and $\boldsymbol{\widetilde{d_{cq}}}$ are small, the product of them can be neglected:

$$\boldsymbol{e^{j\Delta\theta}d_{cdq}} = (\boldsymbol{I} + \boldsymbol{J}\Delta\theta)\left(\begin{bmatrix} D_{cd} \\ D_{cq} \end{bmatrix} + \begin{bmatrix} \widetilde{d_{cd}} \\ \widetilde{d_{cq}} \end{bmatrix}\right) \approx \begin{bmatrix} D_{cd} \\ D_{cq} \end{bmatrix} + \boldsymbol{J}\begin{bmatrix} D_{cd} \\ D_{cq} \end{bmatrix}\Delta\theta + \begin{bmatrix} \widetilde{d_{cd}} \\ \widetilde{d_{cq}} \end{bmatrix} \tag{9.11}$$

Hence, the small signal component of $e^{j\Delta\theta}d_{cdq}$ is given by:

$$\widetilde{e^{\boldsymbol{J\Delta\theta d_{cdq}}}} \approx \boldsymbol{J}\begin{bmatrix} D_{cd} \\ D_{cq} \end{bmatrix}\Delta\theta + \begin{bmatrix} \widetilde{d_{cd}} \\ \widetilde{d_{cq}} \end{bmatrix} \tag{9.12}$$

Based on these assumptions and simplifications, the small signal model of the Vienna rectifier is obtained and is depicted in Fig. 9.32.

The input impedance of the Vienna rectifier with the control loop can be obtained after deriving the transfer function of the SRF-PLL. A block diagram of the SRF-PLL is depicted in Fig. 9.33.

Based on the linearization method given by Eq. (9.10), the transfer function of the small signal model of the SRF-PLL can be derived as:

$$T_{PLL}(s) = \frac{\Delta\theta}{\widetilde{V_{sq}}} = \frac{G_{PLL}(s)}{1 + V_1 G_{PLL}(s)}, G_{PLL}(s) = \frac{k_{pPLL}s + k_{iPLL}}{s^2} \tag{9.13}$$

where k_{pPLL} and k_{iPLL} are the parameters of the PI compensator of the SRF-PLL and V_1 is the amplitude of the fundamental voltage. Finally, the input impedance of the Vienna rectifier is given by:

$$\begin{aligned} \boldsymbol{Z_{in,dq}}(s) &= \begin{bmatrix} Z_{dd}(s) & Z_{dq}(s) \\ Z_{qd}(s) & Z_{qq}(s) \end{bmatrix} \\ => &\left(\boldsymbol{I} - V_{dc}\boldsymbol{G}_{\mathbf{del}}(\mathbf{s}+\mathbf{j}\boldsymbol{\omega}_{\mathbf{1}})\boldsymbol{J}\boldsymbol{D}_{\mathbf{cdq}}\boldsymbol{T}^{\mathbf{m}}_{\mathbf{PLL}}(\mathbf{s}) + \boldsymbol{G}_{\mathbf{del}}(\mathbf{s}+\mathbf{j}\boldsymbol{\omega}_{\mathbf{1}})\boldsymbol{H}_{\mathbf{i}}(\mathbf{s})\boldsymbol{J}\boldsymbol{I}_{\mathbf{sdq}}\boldsymbol{T}^{\mathbf{m}}_{\mathbf{PLL}}(\mathbf{s})\right)^{-1} \\ &\boldsymbol{Y}(\mathbf{s}+\mathbf{j}\boldsymbol{\omega}_{\mathbf{1}})^{-1}(\boldsymbol{I} + \boldsymbol{Y}(\mathbf{s}+\mathbf{j}\boldsymbol{\omega}_{\mathbf{1}})\boldsymbol{G}_{\mathbf{del}}(\mathbf{s}+\mathbf{j}\boldsymbol{\omega}_{\mathbf{1}})\boldsymbol{H}_{\mathbf{i}}(\mathbf{s})) \end{aligned} \tag{9.14}$$

where $\boldsymbol{D_{cdq}} = \begin{bmatrix} D_{cd} \\ D_{cq} \end{bmatrix}, \boldsymbol{I_{sdq}} = \begin{bmatrix} I_{sd} \\ I_{sq} \end{bmatrix}$, and $\boldsymbol{T^{m}_{PLL}}(\boldsymbol{s}) = [0 \quad T_{PLL}(s)]$.

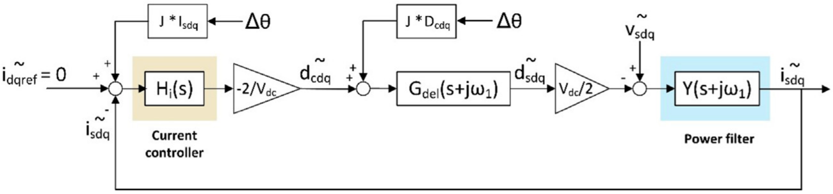

FIGURE 9.32 Small signal model of Vienna rectifier.

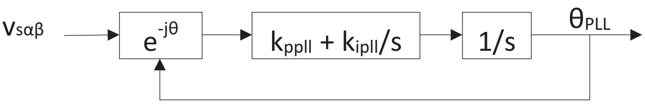

FIGURE 9.33 Block diagram of small signal model of synchronous rotational frame phase locked loop (PLL).

The analytical model of the input impedance of the rectifier given by Eq. (9.14) is in the dq-domain, which does not have a physical meaning. Thus, it is difficult to use the impedance in the dq-domain to evaluate the harmonic current emission of the rectifier induced by the grid harmonic voltage. Hence, the dq-impedance model is transformed to the equivalent sequence impedance model with the method presented in Wang et al. [89]. The derived sequence impedance $Z_{in,\alpha\beta}$ satisfies the equation:

$$\begin{bmatrix} V_{s\alpha\beta}(s) \\ e^{j2\omega_1 t}V_{s\alpha\beta}*(s) \end{bmatrix} = \underbrace{\begin{bmatrix} Z_{+,dq}(s-j\omega_1) & Z_{-,dq}(s-j\omega_1) \\ Z_{-,dq}*(s-j\omega_1) & Z_{+,dq}*(s-j\omega_1) \end{bmatrix}}_{Z_{in,\alpha\beta}} \begin{bmatrix} I_{s\alpha\beta}(s) \\ e^{j2\omega_1 t}I_{s\alpha\beta}*(s) \end{bmatrix} \tag{9.15}$$

$$\begin{aligned} Z_{+,dq}(s) &= \frac{Z_{dd}(s)+Z_{qq}(s)}{2} + j\frac{Z_{qd}(s)-Z_{dq}(s)}{2}, \\ Z_{-,dq}(s) &= \frac{Z_{dd}(s)-Z_{qq}(s)}{2} + j\frac{Z_{qd}(s)+Z_{dq}(s)}{2} \end{aligned} \tag{9.16}$$

The effectiveness of the impedance model can be verified by comparing the model with the frequency sweep with the numerical model. For instance, the analytical model of the Vienna rectifier with the design specifications listed in Table 9.6 is compared with the numerical simulation, which is shown in Fig. 9.34. The model matches well with the simulation results.

The influences of the bandwidth of the PLL and the current loop are also shown in Fig. 9.34. The PLL has more influence on the sequence coupling impedance than the current loop. Moreover, by comparing the solid (blue) line with the dash-dotted (orange) line, it is seen that the PLL influences the sequence impedance mainly in the low-frequency range (i.e., below 500 Hz). On the contrary, the current control loop influences the sequence impedance in

TABLE 9.6 Specifications of Vienna rectifier used as example to show effectiveness of analytical impedance model.

Parameters	**Values**	**Unit**	**Parameters**	**Values**	**Unit**
Line-to-neutral RMS voltage V_g	230	V	Phase locked loop bandwidth *BWPLL*	30	Hz
Inductor L	250	µH	Current loop bandwidth *BWCL*	1000	Hz
Resistor *R*	20	mΩ	Voltage loop bandwidth *BWVL*	500	Hz
Capacitor C_{out}	1500	µF	Switching frequency f_{sw}	20	kHz
DC-link voltage V_{dc}	800	V			

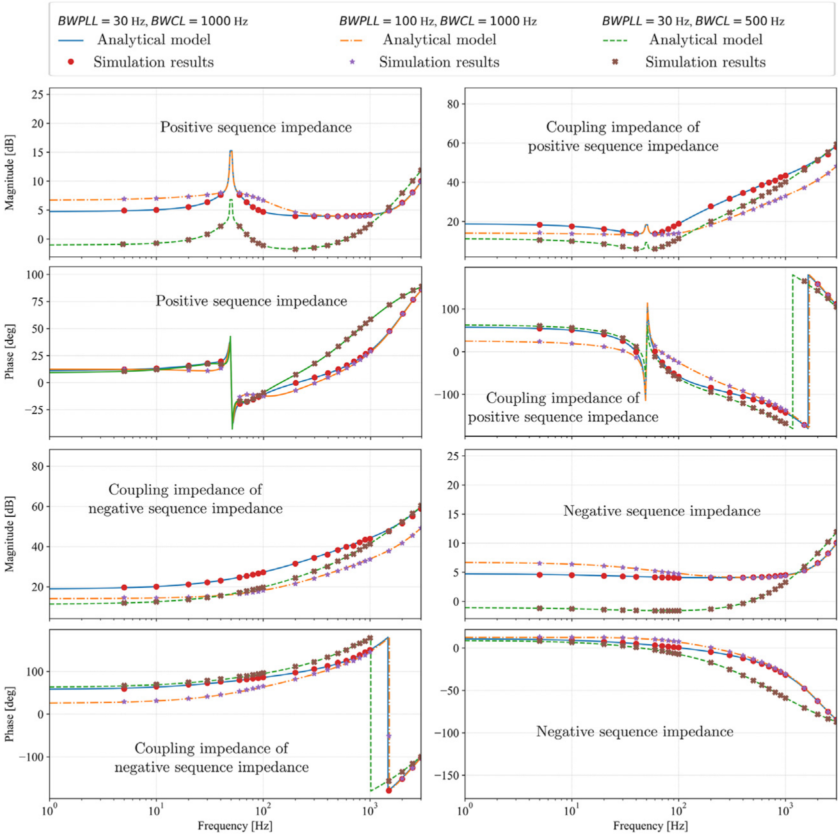

FIGURE 9.34 A decent match between the analytical model of the Vienna rectifier and the simulation result. By comparing the solid (*blue*) line with the dash-dotted (*orange*) line and the dashed (*green*) line, it is clear that, due to the bandwidth selection, the phase locked loop only influences the low-frequency impedance whereas the current loop can influence the input impedance until a higher frequency. For interpretation of the references to color in this figure legend, please refer online version of this title.

a wider frequency range, which is noted by comparing the solid (blue) line with the dashed (green) line in Fig. 9.34. In reality, the control parameters are often not available and it makes the above-mentioned analytical impedance modeling complicated. A gray-box modeling approach addresses this issue by combining the impedance measurement and control parameter extraction [118].

9.6 Smart charging

9.6.1 Definition of smart charging

Smart charging is a series of intelligent functionalities to control the EV charging process to create a flexible, sustainable, inexpensive, and efficient charging environment. It has several benefits and a vast potential for the future. EVs have four unique abilities that make them an excellent asset in the grid: flexibility to vary charging power, flexibility to control the charging time or moments, the ability to ramp up or down charging power quickly, and the ability to both charge and discharge. However, this potential is largely unused. To date, EV charging is an uncontrolled process in which the EV charges at a fixed power once the EV is connected to the charger and charges at the maximum rated power possible based on the charger and EV power rating. Charging continues uninterrupted until the battery is full. Such uncontrolled charging has an adverse impact on the grid in terms of transformer loading, line loading, and nodal voltages due to peak power demanded from the grid [90,92,111,112,115], as shown in Fig. 9.35 [98]. Further impact inlcude the increase the line losses of the grid and harmonic distortion. The kay factors that affects the grid impact of the EVs are the EV penetration level, EV features (EV type, battery size, power rate), grid condition and facilities (Rural/urban, transformer/line capacity, line impedance/length), charging station(-charger) location and charger type (domestic/semi-public/public, power level).

9.6.2 Examples of smart charging

With the use of smart charging, the EV charging power and direction can be continuously controlled (variable power charging). Smart charging of EVs can provide several benefits to the EV owner and to providers of the EV charging infrastructure [99,100]. First, smart charging can balance the local load. This can be achieved in two ways: by shifting the charging time slot according to loading on the grid, or by balancing multiple charge points with priority [94], as shown in Fig. 9.36. This reduces the peak demand on the grid (including on the transformer and lines) and grid losses [113,114].

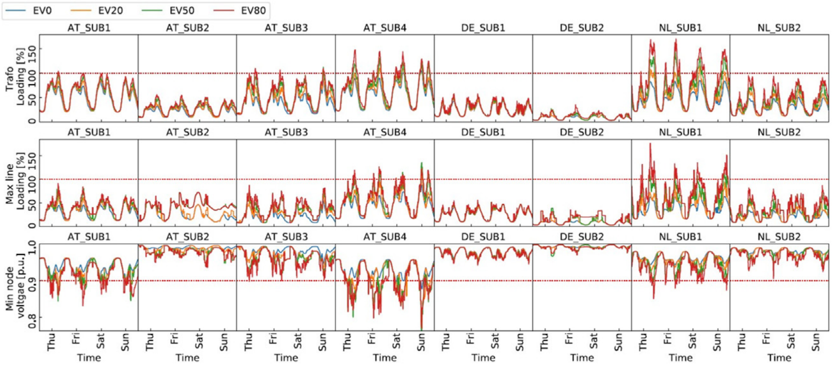

FIGURE 9.35 Impact of uncontrolled charging of electric vehicle (EV) on suburban grid in Austria (AT), Germany (DE), and Netherlands (NL) owing to increasing EV penetration from 0% (EV) to 80% (EV80) in terms of transformer loading, line loading, and nodal voltages [98].

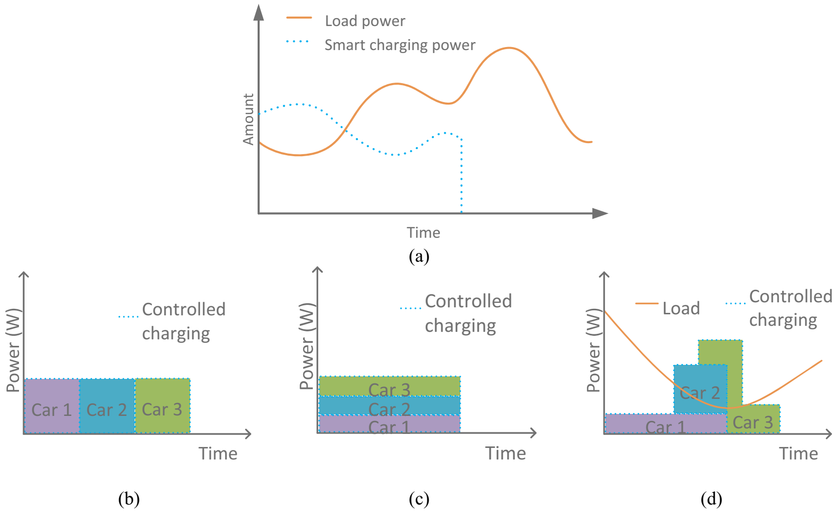

FIGURE 9.36 Smart charging in load balancing of multiple electric vehicles: (A) Charging load shift; (B) Sequential charging to reduce peak power; (C) Simultaneous charging at reduced power; (D) Charging with priority and variable power.

Second, smart charging can increase the use and subsequently the installation of renewable energy sources (RES) in the grid [93,101]. The use of renewable energy such as local solar PV for EV charging has a significant benefits in terms of zero well-to-wheel emissions, reduced charging costs and potentially the reducing the negative impacts of large scale solar and EV penetration [116]. This can be further extended by using EV batteries as short terms energy storage for RES, as shown in Fig. 9.39 [102,103]. Third, smart charging can facilitate charging based on electricity prices to reduce the charging cost, as illustrated in Fig. 9.38 [100,104]. This application is highly related to the electricity market (such as Day ahead market or intra-day market, etc.), which depends on market parties and policies.

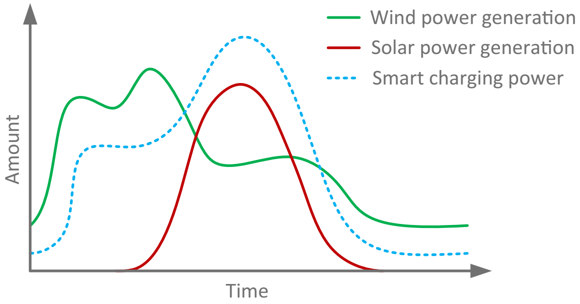

FIGURE 9.37 Smart charging in renewable energy system integration.

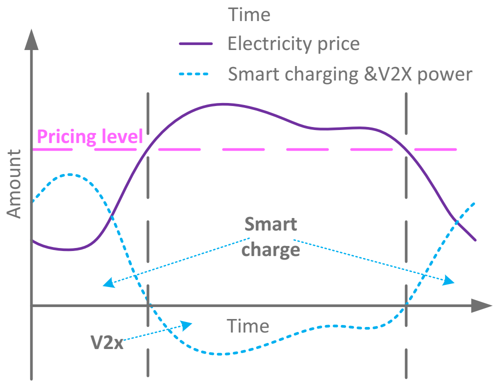

FIGURE 9.38 Smart charging based on energy prices in the electricity market. *EV*, electric vehicle.

Fourth, smart charging can be applied to peak shaving or to provide backup services for the grid, as illustrated in Fig. 9.39. In this case, power flow is bidirectional so that EVs can become a power source when necessary [105].

Other applications of smart charging include voltage support (including reactive power compensation), phase imbalance management, providing frequency response (primary, secondary & tertiary) or reducing the greenhousegas emissions based on the electricity generation mix.

Although smart charging appears always to benefit various actors in the charging system, conflicts of interest among actors can lead to adverse situations. Fig. 9.40 shows how uncontrolled charging (UNC) and three smart

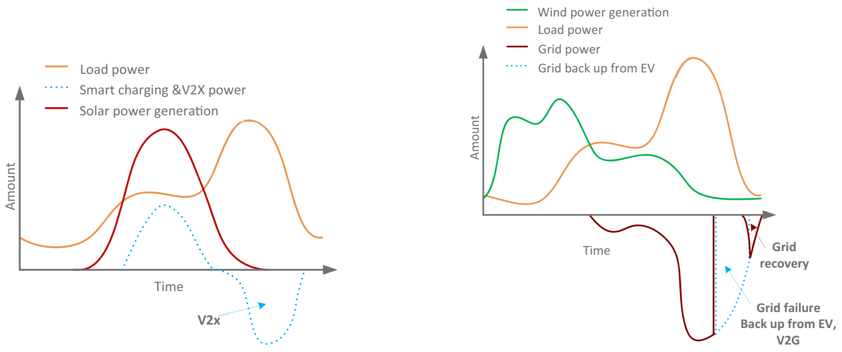

(a) (b)

FIGURE 9.39 Smart charging for grid support: (A) Peak shaving using vehicle to grid (V2G); (B) Grid backup during blackout.

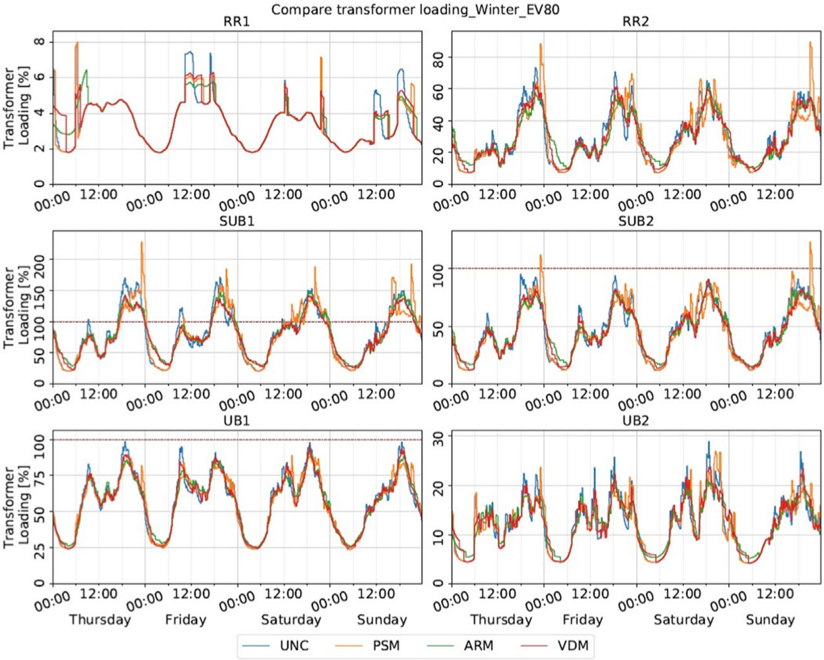

FIGURE 9.40 Impact of three smart charging strategies of electric vehicles (EVs) on transformer loading of two rural (RR), urban (UB), and suburban (SUB) grids in the Netherlands owing to EV penetration of 80% (EV80) in a winter week. Price signal−based charging (PSM) created additional peaks in the grid because of the lack of correlation between electricity markets and grid loading [100]. Uncontrolled charging (UNC), voltage drop based charging (VDM) and average rate charging (ARM) are also shown for reference.

charging strategies, a price signal-based method (PSM) for charging cost reduction, a voltage droop method (VDM) for grid impact mitigation, and the average rate method (ARM) (where the charging power is the ratio of the charging energy demand and the parking time) for a user-centric charging approach can have different impacts on local transformer loading [100]. The PSM creates additional peaks in the grid owing to the lack of correlation between electricity markets and grid loading conditions. On the other hand, the ARM has the least impact on the grid, but it delays charging by the most time from the perspective of the user.

9.6.3 Vehicle to grid

With smart charging or V1G, it is possible to control the time and magnitude of charging power from the power source to the EV. With V2G technology, it is possible to control the time, magnitude, and direction of (dis)charging power [8,9]. An EV can feed power to the home (V2H) or building (V2B), to a load

(V2L), or to the grid (V2G) [106] with all of these applications collectively referred to as Vehicle-to-X (V2X). V2G can be used for all applications of V1G as well as for unique applications such as:

- Short-term storage for renewables such as PV [102–104],
- Higher capacity for frequency regulation, specifically primary and secondary frequency regulation, [102,104]
- Enhanced congestion management with the possibility to feed back power,
- Arbitrage of energy by drawing and feeding power to the grid at moments of different time of use tariffs [101]
- Off-grid or stand-alone applications such as black start, microgrids, or emergency backup power [105]

Challenges to the large-scale adoption of V2G are increased battery degradation [107,108], the higher cost of bidirectional EV chargers compared with unidirectional, required standardization for communication protocol [97], software and charging connectors, potential cybersecurity issues, and the lack of established revenue streams and policy regulations to encourage its use. CHAdeMO has proposed using V2G to provide backup power in case of emergencies [91], more specifically as V2L. The CCS and NACS charging standards are currently in the testing & deployment phases and development phases for V2X, respectively as of 2023. It is expected that with the large-scale use of smart charging, V2G will have a vital role in the future.

9.6.4 Implementing smart charging and vehicle to grid

This section describes how smart charging and V2G can be implemented between the charger and EV for AC and DC chargers.

9.6.4.1 Smart charging via Type 1 and 2 AC charging

Communication and control of the charging process between EV and the charger for AC charging is accomplished using the control pilot (CP) and the proximity pilot (PP). The PP keeps track of the physical connection between the charger and EV, and the CP communicates the maximum capacity of the charger cable. To implement AC smart charging:

- The CP has a PWM signal that can be adjusted to modify the maximum charging current that is available from the charger, shown in Fig. 9.41A as the variable set point.
- Based on the PWM signal on CP, the EV decides the charging current based on the status of the battery, such as the state of charge (SOC) and temperature. Hence, the charging current request is set by the EV, which is the master, and the current requested by the EV can be less than or equal to the maximum charger current. Thus, by controlling the PWM on the CP, smart charging can be implemented.

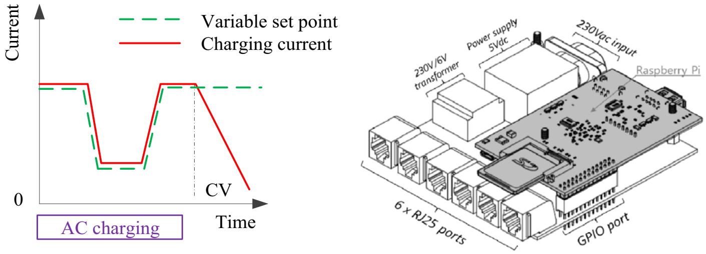

(a) (b)

FIGURE 9.41 (A) Amart charging using AC charging via type 1 or type 2 plug. (B) Three-dimensional rendering of smart charging controller for AC charging. The device collects measurements from current transformers and controls charging power. *CV*, constant voltage [109,110].

- The charger is the slave and supplies current requested by the EV. If the EV battery SOC or temperature is too high, the battery management system of the EV will draw a current lower than the set point. For example, in Fig. 9.41A, the EV SOC is high in the CV region, and the battery goes into CV charging and draws a current that is lower than the set point.
- For example, the smart charging controller developed in [109], shown in Fig. 9.41B, use this technique to charge the EV dynamically based on local PV generation and local residential consumption.

9.6.4.2 Vehicle to grid via type 1 and 2 AC charging

Because EV owners may not be willing to invest separately in a DC charger at home, V2G via onboard AC chargers has an enormous potential for the future. Moreover, the V2G power levels of 10 kW have the same power levels as onboard chargers. However, implementing V2G using AC chargers is currently challenging for two reasons:

1. Most of the EVs on the market are not equipped with bidirectional onboard chargers that support EV discharging. If they do have bidirectional onboard charger, they often provide V2L rather than V2G.
2. The communication protocol based on PWM for AC charging via CP, PP, has no provision for initiating V2G. In the V2G mode, the charger acts like the master and requests the EV to discharge a required amount of current. However, in the current AC charging protocol, the EV is the master, and such a V2G request cannot be enabled.

To overcome these barriers, EV manufacturers should look into installing bidirectional chargers onboard EVs. If communication on the CP, PP, for AC charging can be integrated to include higher level commincation on the CP like PLC as with CCS using ISO 15118 (discussed subsequently), the opportunity for V2G via AC chargers might be realized.

9.6.4.3 Smart charging via CHAdeMO

The CHAdeMO v1.0 charging control mechanism is similar to the AC charging for types 1 and 2. The car is the master. It decides the required charger current and sends a current request command every 200 ms. The charger is the slave and supplies the requested current. The charging protocol is shown in Fig. 9.42A and is:

- The EV and charger make a handshake to:
    - o Share information about the EV, such as the model, battery voltage, and SOC
    - o Set the upper charging current limit based on the maximum charging power of the EV and the charger.
- The EV continuously makes a current set point every 200 ms based on the battery, such as the SOC and temperature.
- The charger has to supply the requested current, with a current resolution of 2.5 A. Thus, charging current supplied by the charger can vary from the set point of the EV by up to 2.5 A.

The maximum current set point of charger and EV set at handshake remains constant throughout for CHAdeMO v1.0. There is no mechanism for the charger to request a change of the maximum limit. Essentially, smart charging is impossible. This is unlike AC charging, in which the upper set point of the charger current can be set continuously with PWM on the CP. Moreover, CHAdeMO v1.0 does not have the facility for V2G, for two reasons. First, v1.0 necessitates the presence of a diode at the charger output, which will allow only charging and not V2G. Second, the communication protocol does not have a facility to make the charger the master to set the charging current and direction. These challenges are overcome in CHAdeMO v1.1 V2G, shown in Fig. 9.42B, where the output diode is not required.

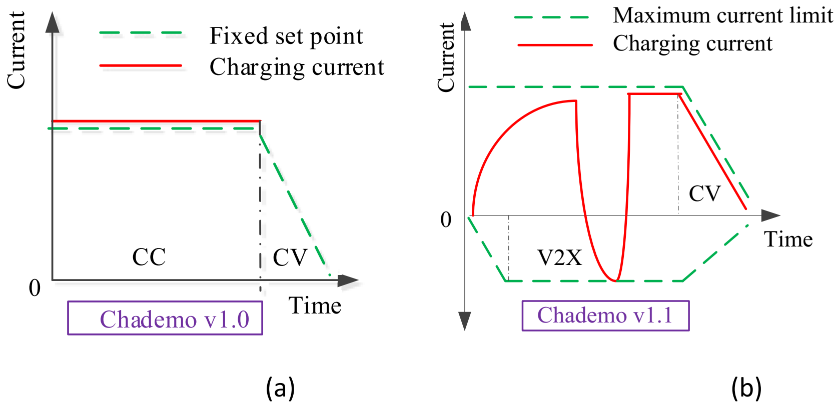

FIGURE 9.42 (A) Conventional charging using CHAdeMO v1.0; (B) Smart charging using CHAdeMO v1.1. *CC*, constant current; *CV*, constant voltage [110].

CHAdeMO v1.1 uses CAN bus signaling, in which EV continuously sets the maximum current for charging and discharging every 200 ms. The following method can be used to implement smart charging using CHAdeMO v1.1 [110]:

- The EV and charger make a handshake to share information about the EV battery. The maximum charging and discharging current is set based on power ratings of the EV and the charger.
- Once charging begins, EV continuously sets the maximum current for charging and discharging every 200 ms, as shown in Fig. 9.40B, based on battery characteristics such as the SOC and temperature. When the maximum discharge current is zero, V2G is is not possible.
- The charger can provide any charging current between the upper and lower bounds with a resolution of 2.5 A. Thus, a varying power such as PV power can be translated into a varying EV charging current as long as it is within the upper and lower bounds. Fig. 9.40B shows that at the start of the graph, the SOC is low and the maximum discharge current (negative limit) is small. The discharge current limit increases as the SOC increases with charging. At the right of the graph, the battery is nearly full, and the maximum charging current limit is slowly reduced by the EV to prevent overcharging the EV batteries.

Hence, CHAdeMO v1.1 facilitates smart charging with high flexibility. A smart energy management system can decide on the optimal charging profile of the EV based on user preferences, energy prices, or renewable generation, and it can be implemented via smart charging.

9.6.4.4 Implementing vehicle to grid using CHAdeMO

Fig. 9.41 shows an experimental setup for implementing V2G using a CHAdeMO-compatible EV [110]. Two separate unidirectional converters are used to charge and discharge the EV battery, respectively, with CHAdeMO implemented on the charge protocol interface. The scope shows the EV battery being charged and then discharged with a current of 4 A. The quick ramp-up and ramp-down of the EV battery at 20 A/s can be observed as well. This exhibits the vast potential of the EV battery to provide a quick response for spinning reserve and frequency regulation applications [8,9,102,104]. With a bidirectional EV charger, even an EV at zero charging power can provide regulation power capacity for both upregulation and downregulation up to the rated power of the charger.

9.6.4.5 Smart charging via CCS/COMBO

CCS/COMBO facilitates smart charging and V2G by using PLC communication over the CP using ISO 15118. This allows high-level communication, overcoming the limitations of using only PWM for communications in AC charging. The implementation of V2G and smart charging for CCS varies from CHAdeMO and is shown in Fig. 9.43 [110]:

- The EV and charger make a handshake to share information about the EV and set the maximum charging current limit based on the power rating of the EV and the charger.
- Once charging begins, the EV and charger continuously negotiate and set a charging and discharging current set point based on battery characteristics such as the SOC and temperature. For V2G or smart charging, the charger can request a change of current, and the EV has to accept this request. Communications are based on ISO 15118.
- If the request is accepted, EV changes the current set point and the charger has to charge or discharge the EV based on the negotiated set point, as shown in Fig. 9.43A. The current resolution is 2.5 A.

Hence, smart charging can easily implemented with CCS, though it is not as flexible as in CHAdeMO. If the EV charging current has to change from I_1 to I_2 owing to a sudden change in renewable generation or energy prices, the EV charger will need to send a request for a new set point, as shown in Fig. 9.43B. It takes time t_1 for the car to respond to the new request, and this changes the set point from I_1 to I_2 over time t_2. For the period $(t_1 + t_2)$, buffer capacity E_{buff} is required to store energy from the renewable source or the grid, based on the EV battery voltage V_{ev}:

$$E_{buff} = V_{ev}(I_1 - I_2)\left(t_1 + \frac{t_2}{2}\right) \tag{9.17}$$

where t_1 and t_2 mainly depend on the manufacturer of the EV, the SOC of the battery, and current set points I_1 and I_2. According to the CCS standard (in 2016), the EV can take up $t_1 = 60$ s to respond to the request for a new current set point from the charger. This is a relatively long response time considering

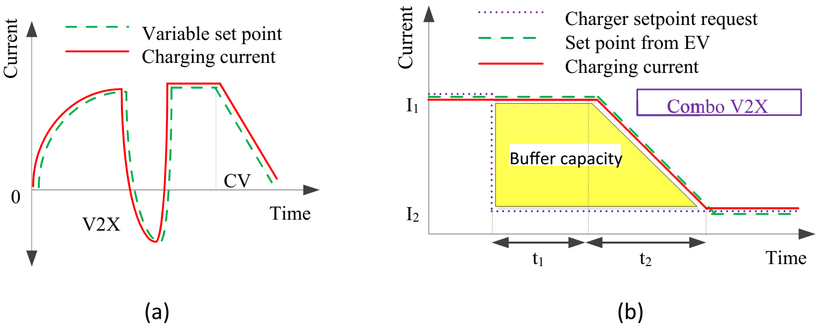

FIGURE 9.43 (A) Smart charging and vehicle to grid using CCS/Combo; (B) Time delays in execution of smart charging and required buffer capacity. *CV*, constant voltage; *EV*, electric vehicle [110].

that many V2G or smart charging applications such as grid ancillary services require the EV to respond within few seconds (≤ 2 s). Also, the CCS standard (in 2016) is silent regarding the time limit t_2 that can be taken by the EV to change the current set point from I_1 to I_2. t_2 can be 10 s or more, as shown in the next section. Both of these are serious drawbacks from the point of view of smart charging, because the EV is susceptible to having a slow response. On the other hand, this buffer capacity, E_{buff}, is not necessary with CHAdeMO. Although manufacturers can design EVs to respond much quicker, a 60s response time for t_1 and no upper limit for t_2 make the CCS implementation slow in theory and require a large buffer capacity E_{buff}. It is expected that t_1 and t_2 will be significantly reduced in the future.

9.6.5 Smart charging protocols

The implementation of the smart charging algorithm cannot be accomplished without the participation of several critical actors in the system, as shown in Fig. 9.44. Every decision made for smart charging requires close collaboration among different parties. To ensure fast and smooth communication among different parties and provide stable negotiation, command, and transaction service support, several ICT (Information and Communications Technology) protocols have essential roles in the whole procedure, as shown in Figs. 9.44 and 9.45. The use of open protocols give a significant benefit of standardisation and interoperability between various vendors/service providers [96,97]. Key protocols are:

- Open Clearing House Protocol (OCHP) - Used between the Charge Point Operator (CPO) and the eMSP (via the clearing house)
- Open Charge Point Interface (OCPI) - Used between the CPO and the eMSP

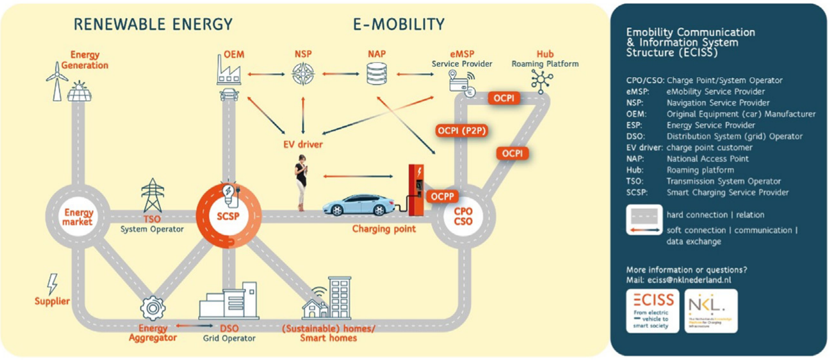

FIGURE 9.44 Electric mobility (E-MOBILITY) Communication and Information System Structure [96]. *OCPI*, open charge point interface.

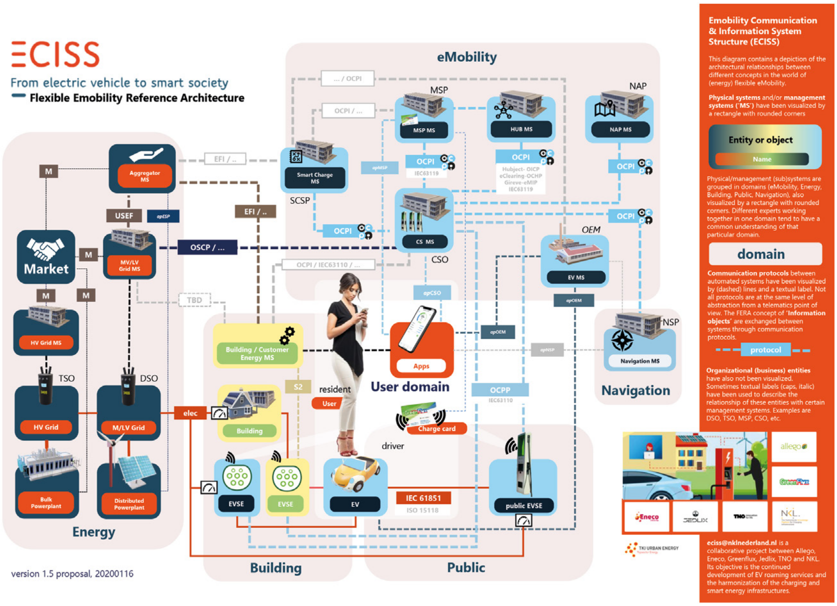

Emobility Communication & Information System Structure (ECISS)

This diagram contains a depiction of the architectural relationships between different concepts in the world of (energy) flexible eMobility.

Physical systems and/or **management systems ('MS')** have been visualized by a rectangle with rounded corners

Physical/management (sub)systems are grouped in domains (eMobility, Energy, Building, Public, Navigation), also visualized by a rectangle with rounded corners. Different experts working together in one domain tend to have a common understanding of that particular domain.

Communication protocols between automated systems have been visualized by (dashed) lines and a textual label. Not all protocols are at the same level of abstraction from a telematics point of view. The FERA concept of '**Information objects**' are exchanged between systems through communication protocols.

Organizational (business) entities have also not been visualized. Sometimes textual labels (caps, italic) have been used to describe the relationship of these entities with certain management systems. Examples are DSO, TSO, MSP, CSO, etc.

eciss@nklnederland.nl is a collaborative project between Allego, Eneco, Greenflux, Jedlix, TNO and NKL. Its objective is the continued development of EV roaming services and the harmonization of the charging and smart energy infrastructures.

version 1.5 proposal, 20200116

FIGURE 9.45 .Market parties and their protocols [96]. *eMIP*, e-Mobility Service Provider; *eMSP*, e-Mobility Service Provider; *DSO*, distribution system operator; *EV*, electric vehicle; *EVSE*, electric vehicle supply equipment; *OCHP*, Open Clearing House Protocol; *OCPI*, Open Charge Point Interface; *OCPP*, Open Charge Point Protocol; *OICP*, Open InterCharge Protocol; *OpenADR*, Open Automated Demand Response; *OSCP*, Open Smart Charging Protocol.

- Open Charge Point Protocol (OCPP) - Used between the CPO and the EVSE
- Open InterCharge Protocol (OICP) - Used between the CPO, clearing house and the eMSP
- Open Automated Demand Response (openADR) - Flexible protocol that can be used between the DSO, EVSE, CSO, EMS, TSO, DSO, Balance responsible party (BRP)
- Open Automated Demand Response (OpenADR)
- Open Smart Charging Protocol (OSCP) - Used between the DSO and the eMSP/CPO
- ISO 15118 - Used for communication between EVs and EVSE.

9.7 Summary

EV charging is becoming an important application of power electronics that increasingly impacts society. Control in EV charging manages the charging performance from the bottom layer (e.g., charging current/voltage, grid side current) to the top layer (e.g., charging time window, charging power, ramping rate of charging power, as well as the PQ on the grid side). Control does not differ much from the low-power (onboard) to the high-power charger (off-board). For a contactless charger, control has to rely on wireless communications for signals transmitted from one side to another at the charging panel, or dual-side control can be applied without communications between the sides. Control of an EV charger can affect its input impedance, which will then influence the PQ. By properly tuning the control parameters, impedance can be reshaped to improve the PQ. The integration of renewables and EV battery charging stations is an attractive concept. A power management strategy is thus needed to take advantage of the battery and reduce the grid connection capacity and cost. Because charging takes a relatively long time (e.g., tens of minutes or hours) and usually is not urgent (e.g., overnight charging, office building charging), it inherently has high flexibility. Smart charging is a series of algorithms that use this flexibility to improve different aspects, including reducing charging costs, shaving peak charging power, and mitigating PQ issues.

References

[1] L. Wang, Z. Qin, T. Slangen, P. Bauer, T. van Wijk, Grid impact of electric vehicle fast charging stations: trends, standards, issues and mitigation measures - an overview 2 (2021) 56−74.

[2] Electric vehicle conductive charging system − Part 1: General requirements, IEC Std. 61851-1 (2017).

[3] M. Yilmaz, P.T. Krein, Review of battery charger topologies, charging power levels, and infrastructure for plug-in electric and hybrid vehicles, IEEE Trans. Power Electron. 28 (5) (2013) 21512169.

[4] A.D.B. Lange, T.B. Soeiro, M.S. Ortmann, M.L. Heldwein, Three-level single-phase bridgeless PFC rectifiers, IEEE Trans. Power Electron. 30 (6) (2015) 2935−2949, https://doi.org/10.1109/TPEL.2014.2322314.

[5] B. Li, F.C. Lee, Q. Li, Z. Liu, Bi-directional on-board charger architecture and control for achieving ultra- high efficiency with wide battery voltage range, in: 2017 IEEE Applied Power Electronics Conference and Exposition (APEC), 2017, pp. 3688−3694.

[6] Z. Qin, Y. Tang, P.C. Loh, F. Blaabjerg, Benchmark of AC and DC active power decoupling circuits for second-order harmonic mitigation in kilowatt-scale single-phase inverters, IEEE Trans. Emerg. Sel. Topics Power Electron. 4 (1) (2016) 15−25.

[7] J. Xu, T.B. Soeiro, F. Gao, H. Tang, P. Bauer, Minimum switching losses discontinuous PWM strategy for bidirectional single-phase AC-DC converter with active power decoupling circuit, IEEE Trans. Power Electron. 36 (5) (2021) 6118−6132.

[8] J. Tomic, W. Kempton, Using fleets of electric-drive vehicles for grid support, J. Power Sources (2007), https://doi.org/10.1016/j.jpowsour.2007.03.010.

[9] W. Kempton, J. Tomic, Vehicle-to-grid power fundamentals: calculating capacity and net revenue, J. Power Sources 144 (1) (2005) 268−279.

[10] T.B. Soeiro, P. Bauer, Fast DC-type electric vehicle charger based on A quasi-direct boost − buck rectifier, in: 2019 AEIT International Conference of Electrical and Electronic Technologies for Automotive (AEIT AUTOMOTIVE), 2019, pp. 1−6.

[11] M. Stecca, T.B. Soeiro, L.R. Elizondo, P. Bauer, P. Palensky, Lifetime estimation of grid-connected battery storage and power electronics inverter providing primary frequency regulation, IEEE Open J. Ind. Electron. 2 (2021) 240–251.

[12] H. Feng, R. Tavakoli, O.C. Onar, Z. Pantic, Advances in high-power wireless charging systems: overview and design considerations, IEEE Trans. Transp. Electrification 6 (3) (2020) 886–919, https://doi.org/10.1109/TTE.2020.3012543.

[13] Z.U. Zahid, et al., Modeling and control of series-series compensated inductive power transfer system, IEEE J. Emerg. Sel. Top. Power Electron. 3 (1) (2015) 111–123, https://doi.org/10.1109/JESTPE.2014.2327959.

[14] Z. Zhou, L. Zhang, Z. Liu, Q. Chen, R. Long, H. Su, Model predictive control for the receiving-side DC-DC converter of dynamic wireless power transfer, IEEE Trans. Power Electron. 35 (9) (2020) 8985–8997, https://doi.org/10.1109/TPEL.2020.296.

[15] T. Diekhans, R.W. De Doncker, A dual-side controlled inductive power transfer system optimized for large coupling factor variations and partial load, IEEE Trans. Power Electron. 30 (11) (2015) 6320–6328, https://doi.org/10.1109/TPEL.2015.2393.

[16] C.H. Dharmakeerthi, N. Mithulananthan, T.K. Saha, Impact of electric vehicle fast charging on power system voltage stability, Int. J. Electr. Power Energy Syst. 57 (2014) 241–249.

[17] S.M. Alshareef, W.G. Morsi, Impact of fast charging stations on the voltage flicker in the electric power distribution systems, in: 2017 IEEE Electrical Power and Energy Conference (EPEC), 2017, pp. 1–6.

[18] T. Thiringer, S. Haghbin, Power quality issues of a battery fast charging station for a fully-electric public transport system in gothenburg city, Batteries 1 (1) (2015) 22–33.

[19] Recommended practice and requirements for harmonic control in electric power systems, IEEE Std. 519 (2014).

[20] IEEE recommended practice for monitoring electric power quality, IEEE Std. 1159 (2019).

[21] IEEE recommended practice for the analysis of fluctuating installations on power systems, IEEE Std. 1453 (2015).

[22] IEEE recommended practice for electric power distribution for industrial plants, IEEE Std. 141 (1993).

[23] Electromagnetic compatibility (EMC) – environment – compatibility levels for low-frequency conducted disturbances and signalling in public low-voltage power supply systems, IEC Std. 61000-2-2 (2002).

[24] Electromagnetic compatibility (EMC) – Part 2–4: environment – compatibility levels in industrial plants for low-frequency conducted disturbances, IEC Std. 61000-2-4 (2002).

[25] Electromagnetic compatibility (EMC) – Part 2–12: environment – compatibility levels for low-frequency conducted disturbances and signalling in public medium-voltage power supply systems, IEC Std. 61000-2-12 (2003).

[26] Electromagnetic compatibility (EMC) – Part 3–4: limits – limitation of emission of harmonic currents in low- voltage power supply systems for equipment with rated current greater than 16 A, IEC Std. 61000-3-4 (1999).

[27] Electromagnetic compatibility (EMC) – Part 3–5: limits – limitation of voltage fluctuations and flicker in low- voltage power supply systems for equipment with rated current greater than 75 A, IEC Std. 61000-3-5 (2009).

[28] Electromagnetic compatibility (EMC) – Part 3–6: limits – assessment of emission limits for the connection of distorting installations to MV, HV and EHV power systems, IEC Std. 61000-3-6 (2008).

[29] Electromagnetic compatibility (EMC) — Part 3—7: limits — assessment of emission limits for the connection of fluctuating installations to MV, HV and EHV power systems, IEC Std. 61000-3-7 (2008).

[30] Electromagnetic compatibility (EMC) — Part 3—13: limits — assessment of emission limits for the connection of unbalanced installations to MV, HV and EHV power systems, IEC Std. 61000-3-13 (2008).

[31] Electromagnetic compatibility (EMC) — Part 3—14: assessment of emission limits for harmonics, interharmonics, voltage fluctuations and unbalance for the connection of disturbing installations to LV power systems, IEC Std. 61000-3-14 (2011).

[32] J. Tan, L. Wang, Real-time charging navigation of electric vehicles to fast charging stations: a hierarchical game approach, IEEE Trans. Smart Grid 8 (2) (2017) 846—856.

[33] T. Zhao, Y. Li, X. Pan, P. Wang, J. Zhang, Real-time optimal energy and reserve management of electric vehicle fast charging station: hierarchical game approach, IEEE Trans. Smart Grid 9 (5) (2018) 5357—5370.

[34] J. Sun, Impedance-based stability criterion for grid-connected inverters, IEEE Trans. Power Electron. 26 (11) (2011) 3075—3078.

[35] J. Lei, Z. Qin, W. Li, P. Bauer, X. He, Modelling of output admittance coupling between shunt active power filters and non-linear loads, in: 2019 4th IEEE Workshop on the Electronic Grid (eGRID), 2019, pp. 1—5.

[36] L. Beloqui Larumbe, Z. Qin, L. Wang, P. Bauer, Impedance modelling for three-phase inverters with double synchronous reference frame current controller in the presence of imbalance, IEEE Trans. Power Electron. (2021), https://doi.org/10.1109/TPEL.2021.3107045.

[37] B. Wen, D. Boroyevich, R. Burgos, P. Mattavelli, Z. Shen, Analysis of d-q small-signal impedance of grid-tied inverters, IEEE Trans. Power Electron. 31 (1) (2016) 675—687.

[38] M. Belkhayat, Stability Criteria for AC Power Systems with Regulated Loads (Ph.D. dissertation), Purdue University, West Lafayette, IN, USA, 1997.

[39] L. Harnefors, X. Wang, A.G. Yepes, F. Blaabjerg, Passivity based stability assessment of grid-connected VSCs—an overview, IEEE Trans. Emerg. Sel. Topics Power Electron. 4 (1) (2016) 116—125.

[40] D. Yang, X. Ruan, H. Wu, Impedance shaping of the gridconnected inverter with LCL filter to improve its adaptability to the weak grid condition, IEEE Trans. Power Electron. 29 (11) (2014) 57955805.

[41] S. Bandyopadhyay, P. Purgat, Z. Qin, P. Bauer, A multiactive bridge converter with inherently decoupled power flows, IEEE Trans. Power Electron. 36 (2) (2021) 2231—2245, https://doi.org/10.1109/TPEL.2020.3006266.

[42] S. Bandyopadhyay, Z. Qin, P. Bauer, Decoupling control of multiactive bridge converters using linear active disturbance rejection, IEEE Trans. Power Electron. 68 (11) (2021) 1068810698, https://doi.org/10.1109/TIE.2020.3031.

[43] T.B. Soeiro, J. Muhlethaler, J. Linner, P. Ranstad, J.W. Kolar, Automated design of a high-power high- frequency LCC resonant converter for electrostatic precipitators, IEEE Trans. Ind. Electron. 60 (11) (2013) 4805—4819, https://doi.org/10.1109/TIE.2012.2227897.

[44] J. Jung, H. Kim, M. Ryu, J. Baek, Design methodology of bidirectional CLLC resonant converter for high-frequency isolation of DC distribution systems, IEEE Trans. Power Electron. 28 (4) (2013) 1741—1755.

[45] D. Lyu, T.B. Soeiro, P. Bauer, Impacts of different charging strategies on the electric vehicle battery charger circuit using phase-shift full-bridge converter, in: 2021 IEEE-PEMC, 2021, pp. 256—263.

[46] C. Marxgut, J. Biela, J.W. Kolar, Interleaved Triangular Current Mode (TCM) resonant transition, single phase PFC rectifier with high efficiency and high power density, in: The 2010 International Power Electronics Conference - ECCE ASIA, 2010, p. 172.

[47] P. Papamanolis, F. Krismer, J.W. Kolar, 22 kW EV battery charger allowing full power delivery in 3- phase as well as l-phase operation, in: 2019 10th International Conference on Power Electronics and ECCE Asia (ICPE 2019 − ECCE Asia), 2019, pp. 1−8.

[48] J. Xu, T.B. Soeiro, F. Gao, H. Tang, P. Bauer, Carrier-based generalized discontinuous PWM strategy for single-phase three-legs active power decoupling converters, IEEE Trans. Ind. Electron. 68 (11) (2021) 11609−11613.

[49] A.M. Hava, R.J. Kerkman, T.A. Lipo, A high-performance generalized discontinuous PWM algorithm, IEEE Trans. Ind. Appl. 34 (5) (1998) 1059−1071.

[50] J.W. Kolar, H. Ertl, F.C. Zach, Realization considerations for unidirectional three-phase PWM rectifier systems with low effects on the mains, in: Proceedings of the 6th International Conference on Power Electronics and Motion Control, Budapest, 1990, pp. 560−565.

[51] M. Hartmann, J. Miniboeck, J.W. Kolar, A three-phase delta switch rectifier for more electric aircraft applications employing a novel PWM current control concept, in: Proceedings of the 24th Annual IEEE Applied Power Electronics Conference and Exposition (APEC 2009), 2009.

[52] T.B. Soeiro, M.S. Ortmann, M.L. Heldwein, Three-phase unidirectional delta-switch multistate switching cells-based multilevel rectifier, in: Proceedings of the 17th European Conference on Power Electronics and Applications (EPE), 2015.

[53] J.W. Kolar, F.C. Zach, A novel three-phase utility interface minimizing line current harmonics of high-power Telecommunications rectifier modules, in: Proceedings of the 16th IEEE International Telecommunications Energy Conference, Vancouver, Canada, 1994.

[54] R.M. Burkart, J.W. Kolar, Comparative life cycle cost analysis of Si and SiC PV converter systems based on advanced η- ρ-σ multiobjective optimization techniques, IEEE Trans. Power Electron. 32 (6) (2017) 4344−4358.

[55] T.B. Soeiro, T. Friedli, J.W. Kolar, Swiss rectifier — a novel three-phase buck-type PFC topology for electric vehicle battery charging, in: 2012 Twenty-Seventh Annual IEEE Applied Power Electronics Conference and Exposition (APEC), 2012, pp. 2617−2624.

[56] T.B. Soeiro, T. Friedli, J.W. Kolar, Design and implementation of a three-phase buck-type third harmonic current Injection PFC rectifier SR, IEEE Trans. Power Electron. 28 (4) (2013) 1608−1621.

[57] L. Schrittwieser, M. Leibl, M. Haider, F. Thony, J.W. Kolar, T.B. Soeiro, 99.3% efficient three-phase buck-type all-SiC SWISS rectifier for DC distribution systems, IEEE Trans. Power Electron. 34 (1) (2019) 126−140.

[58] L.K. Ries, T.B. Soeiro, M.S. Ortmann, M.L. Heldwein, Analysis of carrier-based PWM patterns for a three-phase five-level bidirectional buck- + boost-type rectifier, IEEE Trans. Power Electron. 32 (8) (2017) 6005−6017.

[59] T.B. Soeiro, M.L. Heldwein, J.W. Kolar, Three-phase modular multilevel current source rectifiers for electric vehicle battery charging systems, in: 2013 Brazilian Power Electronics Conference, 2013, pp. 623−629.

[60] S. Manias, P.D. Ziogas, A novel sinewave in AC to DC converter with high frequency transformer isolation, IEEE Trans. Ind. Electron. 32 (4) (1985) 430−438.

[61] V. Vlatkovic, D. Borojevic, F.C. Lee, A zero-voltage switched, three-phase isolated PWM buck rectifier, IEEE Trans. Power Electr. 10 (2) (1995) 148−157.

[62] F. Grazian, W. Shi, J. Dong, P. van Duijsen, T.B. Soeiro, P. Bauer, Survey on standards and regulations for wireless charging of electric vehicles, in: Proceedings of AEIT'2019, 2019, pp. 1−5.

[63] W. Zhang, C.C. Mi, Compensation topologies of high-power wireless power transfer systems, IEEE Trans. Veh. Technol. 65 (6) (2016) 4768−4778.

[64] S. Kim, G.A. Covic, J.T. Boys, Comparison of tripolar and circular pads for IPT charging systems, IEEE Trans. Power Electron. 33 (7) (2018) 6093−6103.

[65] S. Bandyopadhyay, P. Venugopal, J. Dong, P. Bauer, Comparison of magnetic couplers for IPT-based EV charging using multi-objective optimization, IEEE Trans. Veh. Technol. 68 (6) (2019) 5416−5429.

[66] W. Shi, et al., Design of a highly efficient 20 kW inductive power transfer system with improved misalignment performance, IEEE Trans. Transp. Electrification 8 (2021) 2384−2399.

[67] S. Chopra, P. Bauer, Analysis and design considerations for a contactless power transfer system, in: 2011 IEEE 33rd International Telecommunications Energy Conference (IN$^{\mathrm{TEL}}$EC), October 2011, pp. 1−6.

[68] S. Li, W. Li, J. Deng, T.D. Nguyen, C.C. Mi, A double-sided LCC compensation network and its tuning method for wireless power transfer, IEEE Trans. Veh. Technol. 64 (6) (2015) 2261−2273.

[69] Z. Yan, et al., Fault-tolerant wireless power transfer system with a dual-coupled LCC-S topology, IEEE Trans. Veh. Technol. 68 (12) (2019) 11838−11846.

[70] W.-J. Gu, K. Harada, A new method to regulate resonant converters, IEEE Trans. Power Electron. 3 (4) (1988) 430−439.

[71] F. Grazian, W. Shi, T.B. Soeiro, J. Dong, P. Bauer, Electric vehicle charging based on inductive power transfer employing variable compensation capacitance for optimum load matching, in: Proceedings of IECON 2020, 2020, pp. 5262−5267.

[72] H. Feng, T. Cai, S. Duan, X. Zhang, H. Hu, J. Niu, A dual-side-detuned series-series compensated resonant converter for wide charging region in a wireless power transfer system, IEEE Trans. Ind. Electron. 65 (3) (2018) 2177−2188.

[73] F. Grazian, P. van Duijsen, T.B. Soeiro, P. Bauer, Advantages and tuning of zero voltage switching in a wireless power transfer system, in: 2019 IEEE PELS Workshop on Emerging Technologies: Wireless Power Transfer (WoW), 2019, pp. 367−372.

[74] F. Grazian, T.B. Soeiro, P. van Duijsen, P. Bauer, Auto-resonant detection method for optimized ZVS operation in IPT systems with wide variation of magnetic coupling and load, IEEE Open J. Ind. Electron. Soc. 2 (2021) 326−341.

[75] W. Shi, J. Deng, Z. Wang, X. Cheng, The start-up dynamic analysis and one cycle control-PD control combined strategy for primary-side controlled wireless power transfer system, IEEE Access 6 (2018) 14439−14450.

[76] R. Bosshard, J.W. Kolar, B. Wunsch, Control method for Inductive Power Transfer with high partialload efficiency and resonance tracking, in: 2014 International Power Electronics Conference (IPEC-Hiroshima 2014 - ECCE ASIA), May 2014, pp. 2167−2174.

[77] W. Shi, J. Dong, T.B. Soeiro, J. Deng, C. Riekerk, P. Bauer, Continuous reduced-order dynamic model based on energy balancing for inductive power transfer systems, IEEE Trans. Power Electron. 37 (2022) 9959−9971.

[78] H. Hao, G.A. Covic, J.T. Boys, An approximate dynamic model of LCL- T-based inductive power transfer power supplies, IEEE Trans. Power Electron. 29 (10) (2014) 5554−5567.

[79] J.C. Das, Power System Harmonics and Passive Filter Designs, John Wiley & Sons, 2015.

[80] J.H.R. Enslin, P.J.M. Heskes, Harmonic interaction between a large number of distributed power inverters and the distribution network, IEEE Trans. Power Electron. 19 (6) (2004) 15861593.

[81] L. Beloqui Larumbe, Z. Qin, P. Bauer, Introduction to the analysis of harmonics and resonances in large offshore wind power plants, in: 2018 IEEE 18th International Power Electronics and Motion Control Conference (PEMC), August 2018, pp. 393−400.

[82] M. Bollen, S. Ronnberg, Propagation of Supraharmonics in the Low Voltage Grid, Energiforsk, Stockholm, 2017 [Online]. Available: https://energiforskmedia.blob.core.windows.net/media/23665/propagation-of-supraharmonics-in,"the-low-voltage-grid-energiforskrapport-2017-461.pdf. (Accessed 24 May 2020).

[83] J. Sun, Small-signal methods for AC distributed power systems-a review, IEEE Trans. Power Electron. 24 (11) (2009) 2545−2554.

[84] X. Wang, F. Blaabjerg, Harmonic stability in power electronicbased power systems: concept, modeling, and analysis, IEEE Trans. Smart Grid 10 (3) (2019) 2858−2870.

[85] S. Rivera, S. Kouro, S. Vazquez, S.M. Goetz, R. Lizana, E. Romero-Cadaval, Electric vehicle charging infrastructure: from grid to battery, IIEEE Ind. Electron. Mag. 15 (2) (2021) 37−51.

[86] R. Lai, F. Wang, R. Burgos, D. Boroyevich, D. Jiang, D. Zhang, Average modeling and control design for VIENNA-type rectifiers considering the DC-link voltage balance, IEEE Trans. Power Electron. 24 (11) (2009) 2509−2522.

[87] I. Vieto, J. Sun, Sequence impedance modeling and converter-grid resonance analysis considering DC bus dynamics and mirrored harmonics, in: 2018 IEEE 19th Workshop on Control and Modeling for Power Electronics (COMPEL), June 2018, pp. 1−8.

[88] M. Cespedes, J. Sun, Impedance modeling and analysis of grid-connected voltage-source converters, IEEE Trans. Power Electron. 29 (3) (2014) 1254−1261.

[89] X. Wang, L. Harnefors, F. Blaabjerg, Unified impedance model of grid-connected voltage-source converters, IEEE Trans. Power Electron. 33 (2) (2018) 1775−1787.

[90] M.A. Pai, A.M. Stankovic, Electric Vehicle Integration into Modern Power Networks, Springer New York, New York, NY, 2013.

[91] CHAdeMO Association, Technical specifications of quick charger for the electric vehicle, CHAdeMO Protocol (2010-2023).

[92] G.R. Chandra Mouli, P. Bauer, T. Wijekoon, A. Panosyan, E.-M. Barthlein, Design of a power- electronic-assisted OLTC for grid voltage regulation, IEEE Trans. Power Deliv. 30 (3) (2015) 1086−1095.

[93] G.R. Chandra Mouli, P. Bauer, M. Zeman, System design for a solar powered electric vehicle charging station for workplaces, Appl. Energy 168 (2016) 434−443.

[94] H. Zhang, Z. Hu, Z. Xu, Y. Song, Optimal planning of PEV charging station with single output multiple cables charging spots, IEEE Trans. Smart Grid 8 (5) (2017) 2119−2128.

[95] Deleted in Review.

[96] Emobility Communication and Information System Structure (ECISS). [Online]. Available: https://nklnederland.nl/wp-content/uploads/2021/05/ECISS_D1_1_architecture_v1.5.pdf; https://evroaming.org/eciss-communication-structure-for-smart-electric-mobility/.

[97] ElaadNL, EV Related Protocol Study, 2017.

[98] Y. Yu, et al., Data-driven study of low voltage distribution grid behaviour with increasing electric vehicle penetration, IEEE Access (2022).

[99] G.R. Chandra Mouli, et al., Future of electric vehicle charging, International Symposium on Power Electronics (Ee) (2017), https://doi.org/10.1109/PEE.2017.8171657.

[100] Y. Yu, et al., Comparative impact of three practical electric vehicle charging scheduling schemes on low voltage distribution grids, Energies (2022), https://doi.org/10.3390/en15228722.

[101] D. van der Meer, et al., Energy management system with PV power forecast to optimally charge EVs at the workplace, IEEE Trans. Industr. Inform. (2018).

[102] G.R. Chandra Mouli, et al., Integrated PV charging of EV fleet based on energy prices, V2G, and offer of reserves, IEEE Trans. Smart Grid (2019).

[103] G.R. Chandra Mouli, et al., A 10 kW solar-powered bidirectional EV charger compatible with Chademo and COMBO, IEEE Trans. Power Electron. (2019).

[104] W. Vermeer, et al., Optimal sizing and control of a PV-EV-BES charging system including primary frequency control and component degradation, IEEE Open J. Industr. Electron. Soc. 3 (2022).

[105] G. Rituraj, et al., A comprehensive review on off-grid and hybrid charging systems for electric vehicles, IEEE Open J. Industr. Electron. Soc. (2022).

[106] D. Tuttle, The evolution of plug-in electric vehicle-grid interactions, IEEE Trans. Smart Grid 3 (2012).

[107] C. Birkl, et al., Degradation diagnostics for lithium ion cells, J. Power Sour. (2017).

[108] W. Vermeer, et al., A comprehensive review on the characteristics and modeling of Lithium-ion battery aging, IEEE Trans. Transport. Electrif. 8 (2022), https://doi.org/10.1109/TTE.2021.3138357.

[109] B. Bakolas, et al., Testing of smart charging controller for dynamic charging from solar panels, 2014 IEEE Transportation Electrification Conference and Expo (ITEC) (2014), https://doi.org/10.1109/ITEC.2014.6861810.

[110] G.R. Chandra Mouli, et al., Implementation of dynamic charging and V2G using Chademo and CCS/Combo DC charging standard, 2016 IEEE Transportation Electrification Conference and Expo (ITEC) (2016).

[111] R. Green, et al., The impact of plug-in hybrid electric vehicles on distribution networks: A review and outlook, Renew. Sustain. Energy Rev. (2011), https://doi.org/10.1016/j.rser.2010.08.015.

[112] N. Damianakis, et al., Assessing the grid impact of Electric Vehicles, Heat Pumps & PV generation in Dutch LV distribution grids, Appl. Energy (2023).

[113] E. Sortomme, et al., Coordinated charging of plug-in hybrid electric vehicles to minimise distribution system losses, IEEE Trans. Smart Grid (2011), https://doi.org/10.1109/TSG.2010.2090913.

[114] V.V. Ashok, et al., Using dedicated EV charging areas to resolve grid violations caused by renewable energy generation, IEEE Transportation Electrification Conference and Expo (ITEC) (2016), https://doi.org/10.1109/ITEC.2016.7520231.

[115] J. Lopes, et al., Integration of electric vehicles in the electric power system, Proc. IEEE (2011), https://doi.org/10.1109/JPROC.2010.2066250.

[116] G.R. Chandra Mouli, et al., Economic and CO_2 emission benefits of a solar powered electric vehicle charging station for workplaces in the Netherlands, IEEE Transportation Electrification Conference and Expo (ITEC) (2016).

[117] A. Ahmad, Z. Qin, T. Wijekoon, et al., An overview on medium voltage grid integration of ultra-fast charging stations: current status and future trends, IEEE Open J. Ind. Electron. Soc. 3 (2022) 420−447.

[118] L. Wang, Z. Qin, et al., A gradient-descent optimization assisted gray-box impedance modeling of EV chargers, IEEE Trans. Power Electron. 38 (7) (2023) 8866−8879. In press.